Estimating urban seismic damages and debris from building-level simulations: Application to the city of Beirut, Lebanon

Rouba Iskandar, Bilal Al Tfaily, Cécile Cornou, Pierre-Yves Bard, Bertrand Guillier, Jacques Harb, Pascal Lacroix, Jocelyne Adjizian-Gérard, Elise Beck, Julie Dugdale, et al.

▶ **To cite this version:**

Rouba Iskandar, Bilal Al Tfaily, Cécile Cornou, Pierre-Yves Bard, Bertrand Guillier, et al.. Estimating urban seismic damages and debris from building-level simulations: Application to the city of Beirut, Lebanon. Bulletin of Earthquake Engineering, 2023, 21, pp.5949-5990. ⟨10.1007/s10518-023-01768-x⟩. ⟨hal-04207340⟩

HAL Id: hal-04207340

https://hal.science/hal-04207340v1

Submitted on 14 Sep 2023

HAL is a multi-disciplinary open access archive for the deposit and dissemination of scientific research documents, whether they are published or not. The documents may come from teaching and research institutions in France or abroad, or from public or private research centers.

L'archive ouverte pluridisciplinaire **HAL**, est destinée au dépôt et à la diffusion de documents scientifiques de niveau recherche, publiés ou non, émanant des établissements d'enseignement et de recherche français ou étrangers, des laboratoires publics ou privés.

Distributed under a Creative Commons CC0 1.0 - Universal - International License

Estimating urban seismic damages and debris from building-level simulations: Application to the city of Beirut, Lebanon

Rouba Iskandar* [1,2,3], Bilal Al Tfaily[1], Cécile Cornou[1], Pierre-Yves Bard[1], Bertrand Guillier[1], Jacques Harb[4], Pascal Lacroix[1], Jocelyne Adjizian-Gérard[5], Elise Beck[2], Julie Dugdale[3], Christelle Salameh[1], Nada Saliba[5], Rita Zaarour[5]

Abstract

The estimation of seismic damages and debris at the urban scale - at a building-by-building level- is challenging for several reasons. First, commonly used methodologies for seismic damage estimation rarely take into account the local site effects, precisely at the building-level. Second, the available methods for debris estimation fail to estimate at the same time the quantity of debris generated per building according to its damage level and the distribution of the debris (extent and height) around buildings. Finally, the lack of comprehensive data on the building stock and the relevant building properties and their taxonomy further increases the complexity of assessing possible earthquake consequences at an urban scale. This paper addresses these challenges and proposes improvements to the assessment of seismic damages and debris from building-level simulations, along with the development of a 3D building model based on satellite images and heterogeneous data. These developments,

[1] Univ. Grenoble Alpes, Univ. Savoie Mont Blanc, CNRS, IRD, Univ. Gustave Eiffel, ISTerre, 38000 Grenoble, France

* Corresponding author: Rouba Iskandar

rouba.iskandar@univ-grenoble-alpes.fr

[2] Univ. Grenoble Alpes, CNRS, Science Po Grenoble, PACTE, 38000 Grenoble, France

[3] Univ. Grenoble Alpes, CNRS, Grenoble INP*, LIG, 38000 Grenoble, France

[4] Notre Dame Louaize, NDU, Department of Civil and Environmental Engineering, Zouk Mosbeh, Lebanon

[5] Univ. Saint-Joseph, Department of Geography, CREEMO, Beirut, Lebanon

applied to the city of Beirut, Lebanon, highlight the control of the site effects on the seismic damage's spatial distribution throughout the city and the large volume and extent of debris to be expected in the city for a strong earthquake.

Keywords

earthquake; seismic damages; debris; OpenStreetMap; machine-learning; very high-resolution satellite images; Beirut, Lebanon

Acknowledgments

We would like to thank the two anonymous reviewers for taking the necessary time and effort to review the manuscript. We also would like to thank the Centre National d'Etudes Spatiales (CNES) that kindly provided the set of very high-resolution Pleiades 1-B satellite images covering Beirut through the DINAMIS project. We also would like to thank Kamel Allaw for his contribution in the satellite images treatment.

1 Introduction

Earthquakes are one of the most devastating natural hazards that cause important loss of life and livelihood especially in dense urban areas located near seismic faults (e.g. Bam, 2003; Haiti, 2010; Christchurch, 2015) (Elnashai and Di Sarno, 2008). Seismic risk is usually evaluated in terms of physical damages and related economic and social losses from probable earthquake shaking. Approaches for assessing seismic damage can be divided into two main categories (Calvi et al., 2006): (1) empirical methods, such as the damage probability matrix (Braga et al., 1982; Whitman, 1973), which correlate the building damage to the macroseismic intensity; (2) mechanical methods, such as the Capacity Spectrum Method (CSM) (Chopra and Goel, 1999; Freeman et al., 2004), which relate the building damage to the building's capacity curve and to the response spectrum, representing the building characteristics and the spectral acceleration as a function of the spectral displacement imposed by the earthquake, respectively. Empirical methods are commonly used for the estimation of seismic damages at the urban and regional scales (e.g. Lantada et al., 2010; Riedel and Guéguen, 2018; Sarris et al., 2010; Silva et al., 2015), as these methods only require a small amount of qualitative data that can be easily acquired at large scale. However, the spatial resolution of such empirical methods is usually restricted to the administrative-level rather than the building-level, due to the use of aggregated census data for building information and of shake-maps for inferring macroseismic intensity (e.g. Wald et al., 2022). Conversely, although analytical methods require more comprehensive data, they provide clear advantages compared to the empirical methods, due to their physics-based approach allowing the estimation of damages at the building-level (Calvi et al., 2006). Particularly, the applicability of the CSM to different characteristics of hazard and building properties made it very popular and it has been adopted in widely-used seismic risk assessment methodologies, such as HAZUS (FEMA, 2012) and Risk-UE (Mouroux and Le Brun, 2006). In order to account for site effects in building damage aggravation, the CSM uses generic response spectra according to soil classifications based on time-averaged shear wave velocities (usually to a depth of 30 m). The use of such response spectra generally fails to represent the actual site

amplification (Luzi et al., 2011; Pitilakis et al., 2004), especially the aggravation of building damages due to the coincidence of the resonance frequency between soils and buildings – also called double-resonance effects – (e.g. Mexico 1985, Mexico 2017; Cetin et al., 2022; Mayoral et al., 2019; Takewaki, 1998).

Recently, Salameh et al. (2017) proposed a seismic damage assessment approach that takes into account the effect of the spectral coincidence between soils and buildings. This approach was developed by simulating the structural displacement of buildings having various mechanical characteristics and typologies for different levels of ground motion and linear and non-linear site responses. To do so, a comprehensive data set of input seismic signals, soil profiles and single degree of freedom (SDOF) oscillators were used. From the structural displacement, a building damage index was defined based on the EMS98 damage levels (Grünthal, 1998), using a 0–4 scale following the RISK-UE project (Lagomarsino and Giovinazzi, 2006) for buildings located on outcropping rock or sediments (Salameh et al., 2017). This allowed calculating the damage increment between soil and rock conditions. Artificial Neural Networks (ANN) were then trained to predict the damage index and damage increment from easily accessible proxies related to input ground motion, soil and building characteristics. The best predictors for building damages were found to be the Peak Ground Acceleration (PGA) on outcropping rock, the ratio between building and site (f_{struct}/f_{soil}) frequencies and the H/V amplitude (A_{0HV}), which can be considered as a proxy for the impedance contrast. The trained ANNs constituted therefore a simple and robust tool to estimate building damages while combining both the spectral content of the ground motion and the dynamic behaviors of the buildings and soils. This approach can be used to estimate damages at the building-scale in large urban areas. The ANNs were tested and applied to the city of Beirut, in Lebanon, which allowed to establish damage index and damage increment maps for different levels of seismic shaking (Salameh et al., 2017). However, the limitations of this approach come from (i) the quantification of the damages in terms of the damage index and damage increment, inconsistent with standard metrics commonly used for the evaluation of building damages (e.g. Lantada et al., 2009), (ii) the limited exploration of input variables related to the seismic motion, as only the PGA was considered, although several studies have found the Peak Ground Velocity (PGV) to be a better proxy for macroseismic intensity than the PGA (e.g. Kästli and Fäh, 2006; Wald et al., 1999). Moreover, another major limitation in the application to Beirut came from the building data set being incomplete. This meant that only damages on the eastern and the north-western parts of the city were calculated, leaving a gap of building damage in the central area of Beirut. The lack of comprehensive datasets containing relevant information on building properties is a common challenge for many countries threatened by seismic risk (Liuzzi et al., 2019). Although building-by-building surveys are usually considered the most complete source for building characterization (Polese et al., 2019), these surveys are often undertaken within limited spatial areas due to their high time and cost demands (Nievas et al., 2022). Recently, novel approaches relying on satellite images and/or open-accessible geospatial data have been developed to set up seismic exposure models (Geiß et al., 2017; Gomez-Zapata et al., 2022; Krayem et al., 2021; Nievas et al., 2022; Sousa et al., 2017; Wieland et al., 2012). Particularly, in countries with limited census data and incomplete building datasets, such as Lebanon, volunteered geographic information, such as the data provided by OpenStreetMap (OSM) are valuable resources for the development of up-to-date building exposure models (e.g. Tumurbaatar et al., 2021).

Moreover, for earthquakes, debris are generated from structural and non-structural components of damaged buildings (Lu et al., 2019). Falling debris can lead to injuries that need hospitalization (Peek-Asa, 2003) and piles of debris on the road network can block vehicle traffic and even pedestrian evacuation paths slowing down the response of emergency services (Gehl et al., 2022; Mesta et al., 2020). While the estimation of debris volume, extent around buildings and height is of critical importance for improving emergency management plans, only a few studies have focused on the estimation of earthquake-generated debris. HAZUS proposes a methodology to estimate the quantity of generated debris considering the building's typology and damage level; however, this methodology does not investigate the spatial distribution of debris outside the building's right-of-way. The spatial distribution of debris is still an open research question (Castro et al., 2019). The most common practice is to estimate the extent of debris around a building as a function of the building height (H). The extent of the debris around buildings when there is a full collapse is usually assumed to follow a triangular distribution with minimum, maximum and mode equal to H/8, H/2 and H/4 respectively (Nishino et al., 2012). In other works, debris is assumed to form an angle of 20° between the front wall and a line that connects the top of the front wall to the farthest point of the debris (Ravari et al., 2016). Argyroudis et al. (2015) proposed a simplified geometrical model to estimate the debris resulting from collapsed buildings, assuming that the debris form a volume with the shape of a triangular prism having its maximum height next to the building. Furthermore, experimental approaches have also been developed to analyze the debris formation due to an earthquake. Domaneschi et al. (2019) used numerical simulations to study different collapse scenarios of masonry buildings. The numerical simulations were validated by experimental tests on a shaking table, allowing deriving a simplified formula relating the geometric properties of the building with the area occupied by debris. However, the main limitation of this study is that it can only be applied for masonry buildings in the case of full building collapse. Santarelli et al. (2018) relied on machine learning tools to identify correlations between the extent of ruins on the streets outside masonry buildings observed in post-earthquake satellite images, and the buildings' vulnerability, seismic magnitude and ratio between the building's height and street width. By relating the debris extent to the building's vulnerability and the seismic magnitude, this approach is one of the few approaches that takes into account the building's damage level for estimating the debris extents. However, the results are expressed in terms of the fraction of the street that is covered by debris, instead of an absolute debris extent, which is difficult to generalize and to apply to studies in which knowing the width of streets is not a viable option.

Given the aforementioned limitations, the objectives of the paper are first to improve the seismic damage prediction of Salameh et al. (2017) by quantifying the building damage in terms of the mean damage instead of the damage index. The performance of the ANNs to predict the mean damage will also be further explored using various combinations of damage predictors. This part will be covered in section 2 of this paper (Fig. 1). Second, a methodology to estimate damage-dependent height and extent of debris around each building is developed and presented in section 3. Finally, from a new 3D building stock model in Beirut derived using volunteered geographic information, satellite images and machine learning tools (section 4), building mean damage and debris maps are estimated at the scale of the city for different seismic scenarios (section 5).

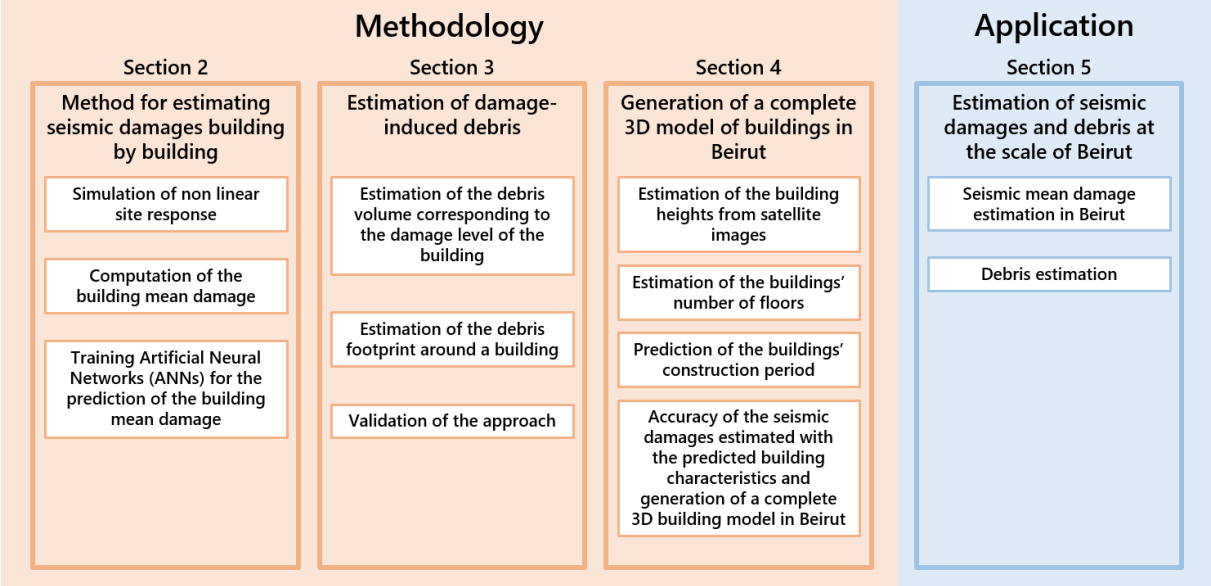

Fig. 1 Pipeline of the framework and organization of the paper

2 Method for estimating seismic damages building by building

A similar approach as in Salameh et al. (2017) was adopted for the estimation of urban seismic damages. The assessment is considered to be at the building level (building by building) because we take into account the spectral contents of both the building and the soil for the estimation of the building damage. We use the same dataset of Salameh et al. (2017) composed of 887 1-D multi-layered soil profiles from worldwide available profiles, 60 synthetic base rock accelerations ranging from 0.02 to 8.6 m/s^2 mimicking accelerations produced by earthquakes with magnitude ranging from 3 to 7 and epicentral distances from 5 to 100 km. Finally, 87 single-degree-of-freedom (SDOF) oscillators exhibiting an elastoplastic behavior and possessing realistic properties were taken into account based on the findings of the Risk-UE European project. In this project, Lagomarsino and Giovinazzi (2006) gathered the principal characteristics of various building types in the Euro-Mediterranean region, including fundamental periods, elastic yield displacement (dy), and ductility ratios (du/dy), where du represents the ultimate displacement. Although these structures were classified by Lagomarsino and Giovinazzi (2006) into five primary building classes encompassing different typologies, in this study we only considered the building classes that can be found in Beirut (Salameh et al., 2017), namely: masonry (Class 1), non-designed reinforced concrete (Class 2), designed reinforced concrete with low ductility (DCL) (Class 3). A comprehensive description of the dataset's characteristics can be found in Salameh (2016).

2.1 Simulation of non-linear site response

Several observations after large earthquakes have found that under strong ground shaking, the soil's behavior becomes nonlinear as it manifests by the shift of the soil's resonance frequency to lower frequencies and the

reduction of the soil's amplification (e.g. Beresnev and Wen, 1996). The soil's nonlinear behavior is a result of the reduction of the soil's shear modulus and the increase in damping that occur when the soil undergoes high deformation levels (Finn, 1991). The soil's nonlinear behavior has also been demonstrated by laboratory tests on different types of soils, which resulted in laws that can be applied for the simulation of the soil's nonlinear behavior (Hardin and Drnevich, 1972a, 1972b). These laws, called degradation curves, relate the loss in shear modulus and the increase in damping to the level of shear strain in the soil. The dynamic soil response can be simulated by fully nonlinear models, such as NOAH (Bonilla, 2001), in which the dynamic equation of motion is integrated in the time-domain at small incremental steps. The computation of the nonlinear soil response can be simplified by an Equivalent Linear (EL) site response analysis, in which the nonlinear soil behavior is simulated by a linear elastic model, with dynamic values of the shear modulus and damping updated iteratively to correspond to the level of strain achieved by the soil according to given degradation curves. Although the EL site response analysis is an approximation of the actual nonlinear response of the soil, this approach has proved to be computationally efficient, capable of providing reasonable results for many practical problems and is widely used by the earthquake-engineering community (e.g. Assimaki et al., 2011; Kaklamanos et al., 2015; Kim et al., 2016).

As the EL approach is less computationally demanding than the full nonlinear method, we have simulated the EL site response of the sites to the input accelerograms. The simulations were performed in SHAKE (Schnabel et al., 1972) that computes the response to vertically propagating plane shear waves of a layered soil profile overlying a uniform half-space. In SHAKE, the soil profile is defined in terms of each sublayer's shear wave velocity, damping ratio, shear modulus and damping degradation curves, total unit weight and thickness. The degradation curves of Darendeli (2001) were used as they are generic curves composed of simple equations, which makes them easy to adapt to any soil type. Nevertheless, the application of Darendeli's relationships requires values of plasticity index and overconsolidation ratios, parameters that are not provided in the soil profiles dataset. Due to the absence of this site-specific information, all the soils were assumed to be dry sand, which yields to values of both plasticity index and overconsolidation ratio equal to 0. The assumption of dry sand is at first order well suited to the study case of Beirut according to the known surface geology (Dubertret, 1945). However, it should be noted that this assumption leads to an exaggeration of the soil's nonlinearity.

The non-linear surface ground motion synthetics were analyzed by calculating the site's transfer function (TF) as the ratio of the Fourier amplitude spectrum of the surface ground motion to that of a reference outcrop rock (Borcherdt, 1970). The TF provides frequency-dependent amplification of the bedrock input motion by the soil deposit (Kramer, 1996). The typical shape of the TF displays many amplification peaks; the peak at the lowest frequency occurs at the site's fundamental resonance frequency. When soils behave nonlinearly under strong ground seismic excitation, the fundamental resonance frequency is decreased together with amplification and de-amplification of the surface ground motion at frequencies below and beyond the fundamental resonance frequency, respectively (Bonilla, 2005; Frankel, 2002; Régnier et al., 2013). Fig. 2 shows the TFs of one of the sites in the dataset, precisely the site AKTH05 from the KiK-Net database (National Research Institute for Earth Science and Disaster Resilience, 2019), computed for the EL soil response for various bedrock accelerations. The TF

corresponding to a linear soil response is also shown for reference. The site response in the EL case depends on the PGA reached at the top of the soil column (surface PGA). While the TFs are relatively close to the linear TF for low-to moderate surface PGA (< 2 m/s^2), the fundamental resonance frequency decreases for larger surface PGA, up to about 20% for the largest surface PGA (from 9 Hz in the linear case to 7 Hz in the non-linear case). The seismic amplification is reduced at the fundamental resonance frequency (by about 10% for the largest surface PGA) and at high frequencies, reaching up to a 40% reduction of the amplification at 20 Hz, while slighter amplification is observed at frequencies below the fundamental resonance frequency.

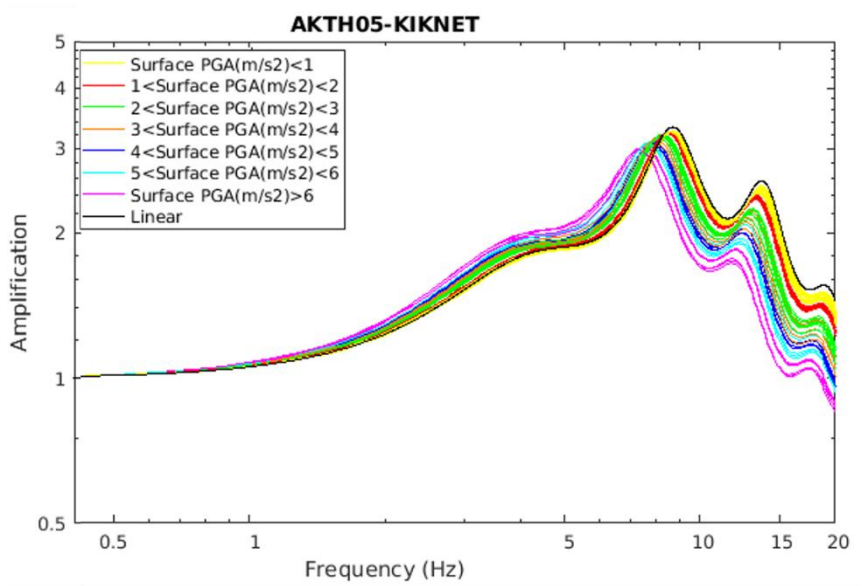

Fig. 2 Site transfer functions for the site ATKH05 from the Kik-Net database computed from the results of the nonlinear site response analysis under 60 different seismic loadings. The site transfer function for the linear site response is plotted in black and the non-linear site responses are indicated in color according to the surface PGA values

2.2 Computation of the building mean damage

The structural displacement was simulated by computing the relative displacement of the damped elastoplastic SDOF oscillators (without including soil-structure interactions for simplification) by solving the dynamic equation of motion using the step-by-step Newmark method:

$$m \times \ddot{d} + c \times \dot{d} + k \times d = -m \times a_{S,i} \quad (1)$$

where d is the displacement in m of the elastoplastic oscillator, $\dot{d}$ its velocity, and $\ddot{d}$ its acceleration. m is the mass in kg, c the viscous damping taken equal to 5%, k the rigidity and $a_{S,i}$ is the surface acceleration in m/s^2 at the base of the oscillator (top of soil column) obtained from the EL calculations.

The building mean damage was then estimated following the mechanical model proposed by Lagomarsino and Giovinazzi (2006). In this approach, four structural displacement thresholds, $S_{d,k}$ (k=1…4), were specified

according to the yielding (d_y) and ultimate (d_u) displacements of the building, which allowed to define four damage states D_{Sk}(k=1...4) as follows:

$$S_{d,1} = 0.7\ d_y\ ;\ D_{S1} = \text{Slight damage}$$

$$S_{d,2} = 1.5\ d_y;\ D_{S2} = \text{Moderate damage}$$

$$S_{d,3} = 0.5(d_y + d_u)\ ;\ D_{S3} = \text{Extensive damage}$$

$$S_{d,4} = d_u;\ D_{S4} = \text{Complete damage}$$

In a second step, the probability that a damage reaches or exceeds a certain damage state D_{Sk}, is expressed as a function of the maximum displacement d_{max} reached by the oscillator and the displacement thresholds $S_{d,k}$, using a lognormal cumulative probability function as follows:

$$P[D_{Sk}|d_{max}] = \Phi\left[\frac{1}{\beta}\ln\left(\frac{d_{max}}{S_{d,k}}\right)\right]\ (k = 1, 2, 3, 4) \tag{2}$$

$$\beta = 0.4\ \ln\mu \tag{3}$$

$$\mu = \frac{d_u}{d_y} \tag{4}$$

where Φ is the normal cumulative function, β is the normalized standard deviation of the natural logarithm of the displacement threshold, defined as a function of μ, the ductility capacity of the building.

Finally, the mean damage (μ_{DS}) is computed as:

$$\mu_{DS} = \sum_{k=0}^{4} kP_{Sk} \tag{5}$$

Where P_{Sk} is the probability of reaching each damage limit state, derived from the cumulative distribution as follows:

$$P_{S4} = P[D_{S4}|d_{max}] \tag{6}$$

$$P_{Sk} = P[D_{Sk}|d_{max}] - P[D_{Sk+1}|d_{max}] \quad (k = 1, 2, 3) \tag{7}$$

$$P_{S0} = 1 - P[D_{S1}|d_{max}] \tag{8}$$

Additionally, the probability of collapse P_5 can be approximated as follows:

$$P_5 = 0.09\ \sinh(0.6\mu_{DS})P_{S4} \tag{9}$$

Moreover, the most probable damage for each value of mean damage was defined as indicated in Table 1 and linked to its corresponding EMS98 damage grade. The probabilities of each damage state according to the mean damage value for classes 1 to 3 can be found in the Appendix (Fig. 21 to 23).

Table 1 Probability of collapse and most probable damage state depending on the mean damage value. The corresponding

EMS98 damage grade is also indicated in the last column

Mean damage	Collapse probability	Most probable damage state	Corresponding EMS98 damage grade
$0 \leq \mu_{DS} < 1$	0	No damage	No damage
$1 \leq \mu_{DS} < 2$	0	Slight DS1	Slight D1
$2 \leq \mu_{DS} < 3$	1% to 9 %	Moderate DS2	Moderate D2
$3 \leq \mu_{DS} < 4$	10% to 48%	Extensive DS3	Heavy D3
$\mu_{DS} = 4$	49 %	Complete DS4	Very heavy D4
			Destruction D5

Table 2 shows the results of the application on the SDOF oscillators and the range of displacements attained along with the corresponding mean damage that ranges between 0 (no damage) and 4 (complete damage state).

Table 2 For each building class, range of fundamental building resonance frequency (f_{struct}), yielding (d_y), ultimate (d_u), maximum (d_{max}) displacement and mean damage (μ_{DS})

Building class	f_{struct} range (Hz)	d_y range (m)	d_u range (m)	d_{max} range (m)	μ_{DS} range
Class 1	2 - 6.7	0.0015-0.0107	0.0070 - 0.0387	1.2477×10^{-5} - 0.5	0 - 4
Class 2	0.77 - 1.85	0.015 - 0.0407	0.0451 - 0.1227	3.8239×10^{-5} - 0.9023	0 - 4
Class 3	1.1 - 2.33	0.0108 - 0.0709	0.0324 - 0.2125	4.3947×10^{-5} - 0.7237	0 - 4

2.3 Training Artificial Neural Networks (ANNs) for the prediction of the building mean damage

The ANN approach is a statistical learning algorithm inspired by biological neural networks. Its main characteristic is investigating, without any *a priori* knowledge, the relationship between input and output variables (McCulloch and Pitts, 1943; Minsky and Papert, 1969). The use of ANNs has emerged in the geophysical field particularly in the early nineties (Poulton, 2001) and has since become a popular tool in solving complex geophysical problems. Following Salameh et al. (2017), we have used ANNs to identify the relationship between the mean damage and indicators related to soil, building and input earthquake signal characteristics. While keeping the same neural network architecture and activation functions, the main changes compared to Salameh et al. (2017) were the choice

of the mean damage as the output variable, instead of damage index, and testing different combinations of input variables as predictors of the mean damage. Moreover, similar to Salameh et al. (2017), the ductility capacity of the buildings was not considered as an input variable in the ANNs; instead, an independent neural network was created for the 3 building typologies used by Salameh (2016) (Class 1, Class 2 and Class 3).

Feedforward neural networks using supervised learning were created using the MATLAB® Neural Network Toolbox™ with the following architecture:

i) an input layer containing the explanatory variables, made of 3 to 5 neurons, depending on the number of explanatory variables considered;
ii) a single hidden layer, containing 10 neurons, which is the optimal number of hidden neurons found after testing numbers between 2 and 20;
iii) an output layer with 1 neuron, containing the variable we aim to estimate, i.e. the mean damage.

The activation functions were the tangential sigmoid activation function in the hidden layer and the linear sigmoid in the output layer. For the choice of damage indicators, in addition to variables used by Salameh et al. (2017), namely PGA, A_{0HV} as the amplitude of the H/V peak at the fundamental resonance frequency, serving as a proxy to site amplification in the linear case, and the ratio between the fundamental resonance frequency of the building (f_{struct}) and the soil (f_{soil}), f_{struct}/f_{soil}, we have also considered f_{struct} and f_{soil} separately. The PGV on outcrop rock was also considered as a proxy of the seismic signal. Eight different combinations of these variables were formed, in a way that each combination included at least one proxy for each of the signals, sites and buildings. Each one of the 8 artificial neural networks was trained for building classes 1, 2 and 3 and the datasets were randomly split into three subsets (70% training, 15% validation set and 15% test set) to avoid overfitting problems. The ANN's performance was assessed by the coefficient of determination R^2 (from 0 to 1), which shows how well the input variables can predict the mean damage.

The ANNs' input variables and performances are summarized in Table 3. All the neural networks performed comparably well in estimating the mean damages, as demonstrated by the high R^2 values ranging from 0.8466 to 0.9602. By comparing the R^2 values in ANN1 and ANN2, the PGV seems to perform better than the PGA in explaining the mean damages, especially for Class 2 buildings. The same applies for the improvement between ANN3 and ANN4, as well as between ANN5 and ANN6. Yet, the consideration of both PGA and PGV simultaneously as proxies of the seismic signal (ANN7 and ANN8) improved the prediction of the mean damages. In ANN3, the consideration of f_{soil} and f_{struct} separately did not lead to the improvement in the R^2 values in any of the classes with respect to ANN1. However, in ANN5, the separation of f_{struct} and f_{soil} without removing A_{0HV} improved the performance for Class 1 but worsened it for the other building classes. Finally, the consideration of all the variables separately in ANN8, improved the prediction of the mean damages for Class 1 compared to ANN7 while the ANN's performance declined for Classes 2 and 3. Finally, while the best performance for Class 1 is achieved in ANN8, ANN7 ensures the best performance for Classes 2 and 3 buildings and was retained as the optimal neural network for the prediction of the building mean damage.

Table 3 Summary of the input variables and the performance of the 8 ANNs trained to estimate the mean damages of building classes 1, 2 and 3. ANN1 is composed of the same input variables as in Salameh et al. (2017). The values of R^2 in bold represent the maximum R^2 attained for each building class

ANN	Nb. of input variables	Input variables	Coefficient of determination R^2		
			Class 1	Class 2	Class 3
ANN1	3	PGA; A_{0HV}; f_{struct}/f_{soil}	0.8778	0.9153	0.8597
ANN2	3	PGV; A_{0HV}; f_{struct}/f_{soil}	0.8793	0.9579	0.8735
ANN3	3	PGA; f_{soil}; f_{struct}	0.8724	0.9038	0.8466
ANN4	3	PGV; f_{soil}; f_{struct}	0.8817	0.9514	0.8662
ANN5	4	PGA; A_{0HV}; f_{soil}; f_{struct}	0.8855	0.9111	0.8551
ANN6	4	PGV; A_{0HV}; f_{soil}; f_{struct}	0.8866	0.9551	0.8785
ANN7	4	PGA; PGV; A_{0HV}; f_{struct}/f_{soil}	0.8957	**0.9602**	**0.8845**
ANN8	5	PGA; PGV; A_{0HV}; f_{soil}; f_{struct}	**0.8981**	0.9594	0.8804

After identifying the optimal neural network, we investigated the input variables' synaptic weights ratio, which is the proportion of the weight of each of the inputs of the ANN with respect to the sum of the total weights in the network. The synaptic weight indicates the relative importance of each input variable in ANN7 in the prediction of the buildings' mean damages. We can see in Fig. 3 that for Class 1 buildings, the PGV has the highest synaptic weight (37.7%), followed by f_{struct}/f_{soil} (29.1%). For Class 2 buildings, f_{struct}/f_{soil} has a higher synaptic weight (38.1%) than the PGV (34.2%), however for Class 3 buildings f_{struct}/f_{soil} is the predominant indicator with a synaptic weight (68.7%), while all the other variables have significantly lower weights. From the synaptic weights distribution, it can be concluded that it is f_{struct}/f_{soil} and the PGV that mostly control the buildings mean damages, followed by the PGA and finally the A0HV, the most vulnerable buildings (Class 1 and Class 2) being however the most sensitive to the level of seismic excitation as a consequence of their related fragility curves.

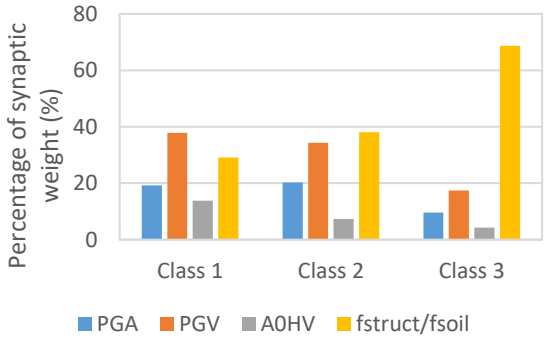

Fig. 3 Synaptic weight proportions for the inputs (PGA, PGV, A_{0HV} and f_{struct}/f_{soil}) of ANN7 for building classes 1, 2 and 3

3 Estimation of damage-induced debris

The literature review identified a gap in models that could estimate the spatial distribution of debris around buildings while also accounting for the severity of the buildings' damage. In order to estimate a damage-dependent height and extent of debris around buildings, we first estimate the volume of generated debris in the case of full collapse. Then, the debris volume corresponding to the building's damage state is estimated using available correlations between the building's damage and the generated debris quantity, and distributed around the building following a geometrical model.

3.1 Estimation of the debris volume corresponding to the damage level of the building

To compute the volume of debris in the case of full collapse, we assumed that when a building collapses, debris are generated from the building's structural elements, specifically the exterior walls and the floor slabs (Fig. 4 (a)). The debris generated from interior walls and partitions, furniture and other objects in the buildings were not considered for simplification purposes. Also for the sake of simplification, buildings were assumed to have a regular rectangular shape. The debris volume in case of total collapse can therefore be computed as:

$$V_t = 2 \times W \times H \times e + 2 \times L \times H \times e + n \times W \times L \times s \quad (10)$$

Where V_t represents the total debris volume in case of full collapse (in m^3), W is the building width (in m), H is the building's height (in m) and L is the building's length (in m). e and s represent respectively the thickness of the exterior walls and the thickness of the floors slabs (in m), while n represents the building's number of floors.

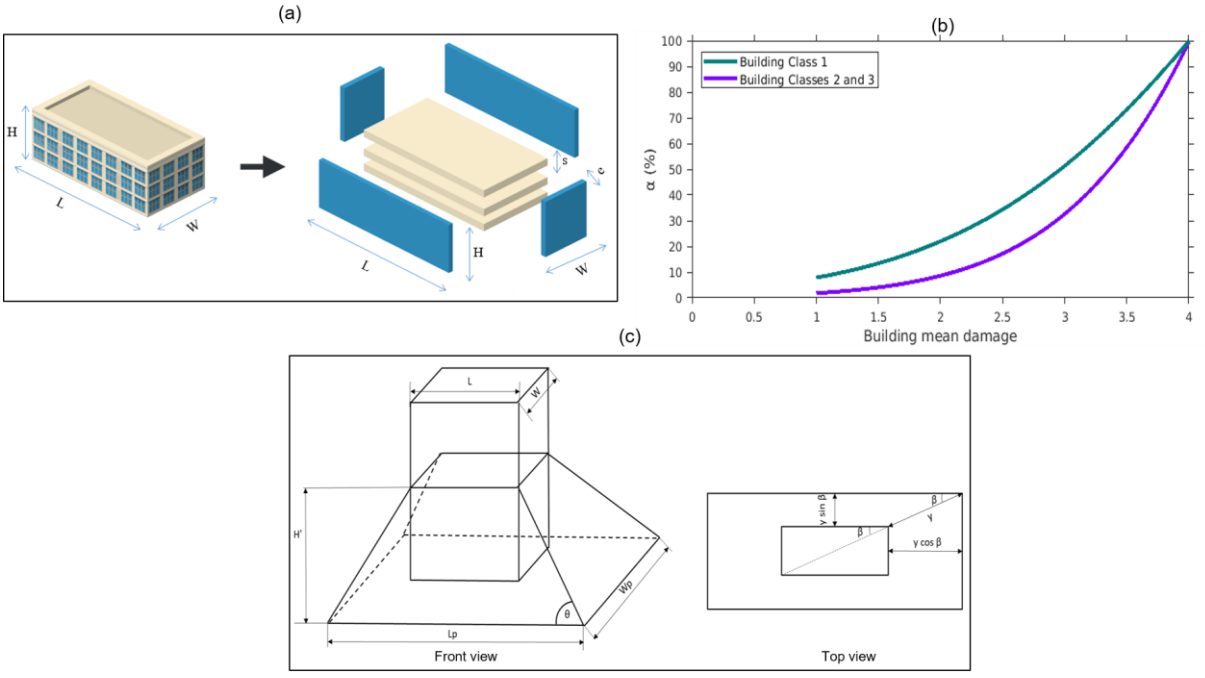

Fig. 4 Debris estimation methodology. (a) Parameters used for the calculation of debris generation from the building's structural

elements. (b) Percentage of total debris (α) generated depending on the mean damage for each building typology. (c) Front and top views of truncated pyramid shaped debris

In case of partial buildings damages, the generated volume of debris was considered to represent fraction of V_t computed as:

$$V_d = \alpha \times V_t \tag{11}$$

Where V_d is the volume of debris corresponding to the mean damage of the building and α is the proportion of total debris volume that is generated at this particular damage level.

In order to determine the fraction of the total debris volume generated according to the damage level, we have relied on the debris estimation method provided by HAZUS (FEMA, 2012), which has compiled tables containing the percentage values of debris weight based on observations of damage caused by previous earthquakes. HAZUS provides estimates of the percentage of debris weight from damaged structural elements depending on factors such as the building typology and the extent of damage. These estimates are provided for two different categories of debris, the first category consisting of brick, wood, and glass while the second category comprises debris generated by steel members and reinforced concrete elements. The values provided by HAZUS could be adopted for the relationship between debris volume and building damage state by assuming that all building materials have the same unit weight. Under this assumption, the percentage of debris volume generated for a given damage level can be considered the same as the percentage of debris weight.

In order to utilize the tables provided by HAZUS, the first step is to establish the correspondence of the building typologies between our approach and HAZUS. Class 1 buildings can directly be considered equivalent to the Unreinforced Masonry Bearing Walls (URM) building type in HAZUS. However, the exact equivalents of classes 2 and 3 could not be found in HAZUS. Firstly, because the building classification in HAZUS does not differentiate between non-designed (class 2) and designed (class 3) reinforced concrete. Secondly, HAZUS differentiates reinforced concrete buildings according to their type of structural system (e.g. moment resisting frame or sheer walls), which we do not do in this study. To overcome these limitations, we have considered that reinforced concrete classes 2 and 3 are equivalent in terms of debris they generate at the same level of building damage. Then, we have identified the most common HAZUS typologies for reinforced concrete buildings in Beirut as Moment Resisting Frame (typology C1 in HAZUS) and Concrete Frame with Unreinforced Masonry Infill Walls (C3 in HAZUS). Finally, we have decided to assign the debris percentages for classes 2 and 3 as the average of the values provided by HAZUS for C1 and C3 buildings.

For the assignment of the debris percentage, we have considered the most probable damage state corresponding to the mean damage value. Then for each damage state, since we do not distinguish between different types of debris, namely debris made of brick or steel and reinforced concrete, we have assigned to each building typology the maximum debris percentage found in HAZUS for the corresponding damage state regardless of the debris type. These values are summarized in Table 4 and Table 5. However, the mean damage computed in the previous section is on a continuous scale from 0 to 4 while the values in Table 4 and Table 5 are given for discrete damage levels.

Therefore, to determine the values of α corresponding to any mean damage value, the data points found in Table 4 and Table 5 were fitted onto a curve using non-linear regression analysis, and the best fit was achieved with a Gaussian curve, which yielded the highest goodness of fit parameters. The values taken for α for each building type for mean damage values ranging from 1 to 4 are displayed in Fig. 4 (b).

Table 4 Percentage of debris weight from damaged structural elements for Class 1 buildings (URM- Unreinforced Masonry Bearing Walls) (adapted from: HAZUS, FEMA 2012)

Mean damage	**Damage state probability**				**Most probable damage state**	**Percentage of debris weight from structural damage state**
	Slight	**Moderate**	**Extensive**	**Complete**		
μ_{DS}**=1**	35% - 61%	11% - 26%	3% - 4%	1%	Slight	**0**
μ_{DS}**=2**	24% - 38%	25% - 44%	18% - 25%	9%	Moderate	**25%**
μ_{DS}**=3**	4% - 10%	17% - 27%	29% - 37%	36%	Extensive	**50%**
μ_{DS}**=4**	0%	0%	0%	100%	Complete	**100%**

Table 5 Percentage of debris weight from damaged structural elements for Class 2 (C1- Reinforced Concrete Moment Resisting Frames) and Class 3 (C3- Concrete Frame Buildings with Unreinforced Masonry Infill Walls) buildings (adapted from: HAZUS, FEMA 2012)

Mean damage	**Damage state probability**				**Most probable damage state**	**Percentage of debris weight from structural damage state**
	Slight	**Moderate**	**Extensive**	**Complete**		
μ_{DS}**=1**	60%	12%	4%	0%	Slight	**0**
μ_{DS}**=2**	38%	26%	25%	8%	Moderate	**12.5%**
μ_{DS}**=3**	10%	17%	37%	36%	Extensive	**30%**
μ_{DS}**=4**	0%	0%	0%	100%	Complete	**100%**

3.2 Estimation of the debris footprint around a building

For estimating the debris footprint around a building, a geometrical model similar to Argyroudis et al. (2015) was developed except that adjacent buildings façades were not considered continuous but separated, thus debris could fall in all four directions around the building. This simplification is motivated by the difficulty of mapping the degree of adjacency of one building to another at the city scale in the absence of detailed building footprint maps. The estimation results in the formation of debris in the shape of a truncated pyramid whose volume is filled by the volume of the generated debris V_d (Fig. 4 (c)). The debris extent around the building can be computed by

calculating the dimensions of the pyramid's base L_p and W_p. The height of the debris at the highest point next to the building façade can also be computed by finding H′, the truncated pyramid's height.

The truncated pyramid's volume is given by:

$$Vp = \frac{H'}{3}\left(B + b + \sqrt{B \times b}\right) \tag{12}$$

$$b = L \times W \tag{13}$$

$$B = Lp \times Wp = (L + 2 \times y \times cos\beta) \times (W + 2 \times y \times sin\beta) \tag{14}$$

$$H' = y \times cos\beta \times tan\theta \tag{15}$$

$$\beta = tan^{-1}\left(\frac{W}{L}\right) \tag{16}$$

where B is the area of the truncated pyramid's base (in m^2), b is the area of the truncated pyramid's top (in m^2) and H′ is the height of the truncated pyramid (in m). In the top view (Fig. 4 (c)), y represents the diagonal distance between the building's corner and the debris' corner (in m). β is the angle between the building's length and its diagonal and θ is the angle between the debris and horizontal plane.

Under the assumption that the debris falls uniformly in all directions, filling the volume of the truncated pyramid:

$$V_p = V_d \tag{17}$$

Solving equation (17) with one unknown, gives the value of y, from which the debris height can be directly calculated as:$y \times cos\beta \times tan\theta$, and the debris extent can be calculated in both directions as: $y \times cos\beta$ and $y \times sin\beta$.

3.3 Validation of the approach

Previous studies highlighted the dependence of the extent of the debris around the building on the building's height. The debris extent was commonly found to be proportional to the building height (H), with values ranging from H/2 to H/8 (Nishino et al., 2012). Since these relationships were established for cases of full building collapse only, the relationship between the debris extent computed using the developed model and the building height was investigated for the case of complete collapse (mean damage = 4).

A rectangular building with dimensions L = 20 m and W = 10 m was considered. The building's number of floors varied from 1 floor to 40 floors, with a floor height set to 3.5 m. The angle at the diagonal of the building was calculated as: $\beta = tan^{-1}(\frac{10}{20})$. The angle θ formed by the debris and the horizontal plane was assumed to be equal to 30°. The thicknesses of the walls and the floor slabs were considered to be respectively e= 0.2 m and s= 0.5 m

The debris extent in the diagonal direction, y, was computed for each building height by solving equation (17). The resulting debris extent is shown in Fig. 5 as a function of the building's height. It can be observed that as the

height of the building increases, the extent of debris away from the building increases as well. For building heights less than 20 m, the debris extent ranges between H/2 and H/4. As the building becomes taller (up to 115.5 m, 33 floors), the debris extent tends gradually away from H/4 and closer to H/8. The debris extent becomes less than H/8 for buildings taller than 115 m. Therefore, in our model, as the building height increases, the ratio between the debris extent and the building height decreases. This observation has not been documented in the literature, as no other study offers a detailed comparison between debris extent and building height. We believe that this is mainly due to the geometrical considerations of the truncated pyramid shape, which highly depends on the ratio between the building's length and width that sets an upper limit to the debris extent.

However, the debris estimated using the developed approach are within the range found in the literature, even though the approach needs to be validated and refined for high-rise buildings by conducting further experiments and collecting post-seismic event observations.

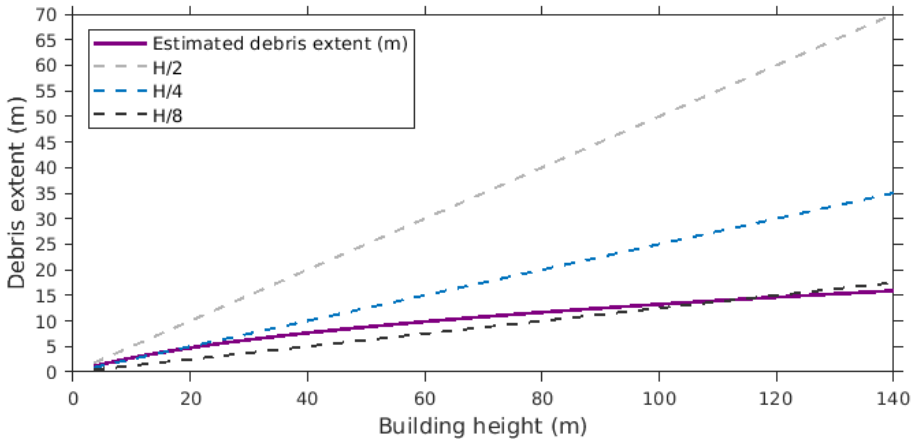

Fig. 5 Comparison of the debris extent estimated for a collapsed building following the developed methodology to the typical relationships with the building height (H) found in the literature

4 Generation of a complete 3D model of buildings in Beirut

In Beirut, a comprehensive building dataset does not exist due to the absence of an up-to-date building census. In the framework of ANR-LIBRIS project (2010 - 2014) (Agence nationale de la recherche, 2010), the Saint Joseph University (USJ) conducted extensive surveys on Beirut's buildings by collecting geographical coordinates, construction year and number of floors of 7 362 buildings (Salameh, 2016). Additionally, ambient noise measurements were carried out on another set of 330 buildings to extract the fundamental resonance frequency of these buildings, in addition to their typology, construction year and number of floors. From the measured resonance frequencies, relationships between the number of floors, soil type and resonance frequency were derived (Salameh et al., 2016) as follows:

- f_{struct} =23/number of floors, for buildings constructed on rock sites;
- f_{struct} =18/number of floors, for buildings built on soft sites.

Moreover, Salameh et al. (2017) proposed a classification of the buildings' typologies based on their number of floors and construction period. Buildings constructed before 1950 with less than 4 floors consisted mainly of masonry buildings (Class 1). Buildings constructed before 1950 with 4 or more floors and buildings constructed between 1950 and 2005 were classified as non-designed reinforced concrete (Class 2). Buildings built after 2005 were considered as designed reinforced concrete with low ductility (Class 3). Indeed, this typology classification is rather simplified compared to other established taxonomies, such as the GEM building taxonomy (Silva et al., 2022) or ESRM20 (Crowley et al., 2020); however, the lack of building census data in Lebanon significantly increase the challenges of having a more refined building characterization. The distribution of the characteristics of the surveyed buildings in Beirut is shown in Appendix (Fig. 24). However, due to security and political constraints at the time of the LIBRIS project, the building survey was restricted to the eastern and north-western sectors of the city as shown in Fig. 6. Since a complete building inventory is essential for estimating building damages throughout the city, we have relied on the existing building dataset, satellite images, and OpenStreetMap (OSM) to generate a 3D building model of Beirut and characterize its typology.

Building footprints in Beirut were already available on OSM at the start of our work. However, we contributed to the completion of the building database on OSM by digitizing the missing buildings, resulting in the delimitation of a total of 15 089 buildings in Beirut. The OSM shapefile layer of buildings in Beirut extracted on 26/02/2021 is displayed in Fig. 7. The estimation of the seismic damages from the OSM dataset requires first the derivation of the buildings' typology and their resonance frequency. Although the LIBRIS dataset contains valuable attributes (construction period and number of floors) for 7 692 of these buildings, these attributes could not be directly transferred to the OSM layer due to georeferencing incompatibilities between the two building layers (see Appendix Fig. 26), caused by the use of a combination of several projection systems when digitizing the building footprints in LIBRIS.

To overcome this limitation and to make use of the information provided in LIBRIS, a subset of 947 buildings from the LIBRIS dataset were manually identified in the OSM dataset by finding the footprints of identical buildings in the two layers. These buildings were selected by picking all buildings that have more than 10 floors in LIBRIS, and a representative set of buildings with lower number of floors. We aimed to sample the overall distribution of number of floors and construction period in the LIBRIS database while selecting buildings in the western and eastern parts of Beirut. The spatial distribution of the selected buildings (referred to as LIB-STAT dataset) is displayed in Fig. 6. The attributes related to the number of floors and the construction year were added to the corresponding OSM buildings. The distribution of the building attributes in the subset of 947 buildings is displayed in Appendix (Fig. 25). This subset is assumed to be representative of Beirut's buildings and was used to derive statistical relationships between different building attributes in order to estimate the OSM buildings' number of floors and construction periods.

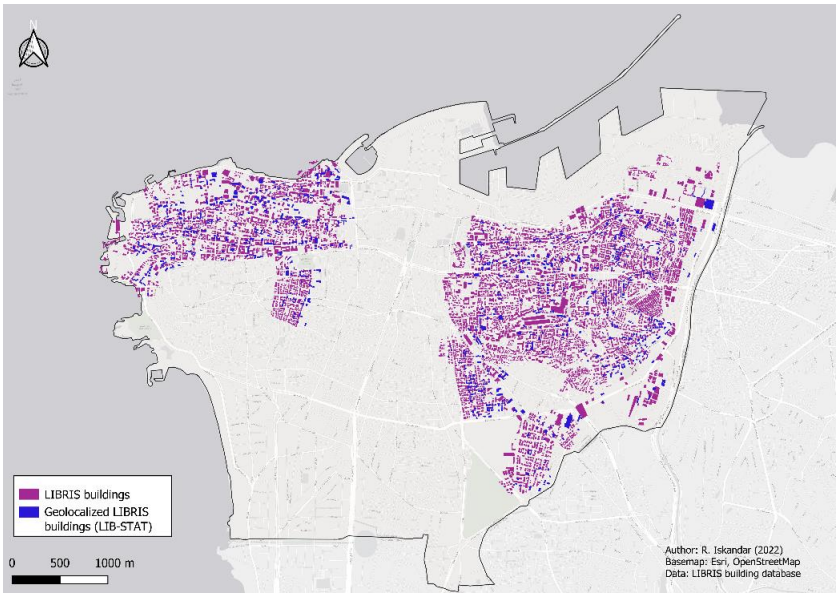

Fig. 6 Buildings in Beirut surveyed during the LIBRIS project and corrected location of 947 of these buildings in blue (LIB-STAT data set)

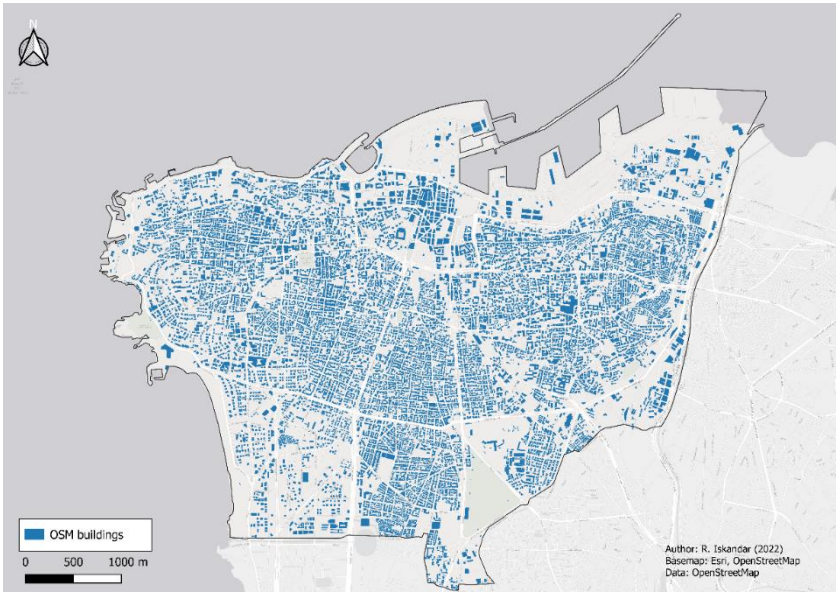

Fig. 7 Buildings footprints in Beirut retrieved from OSM

4.1 Estimation of the building heights from satellite images

The first step for characterizing the building dataset is to retrieve the height of each building, which was done by

processing very high resolution satellite images. Tri-stereo Pleiades 1-B[1] satellite images (resolution 0.7 m) acquired in July 2016 for Beirut and its surroundings (see Appendix Fig. 27) were processed using the Ames Stereo Pipeline software (Broxton and Edwards, 2008), an automated stereo processing software developed by the NASA Ames Research Center, capable of generating high-quality surface elevation models from satellite images. We followed the methodology developed in Lacroix (2016) that can be summarized as follows:

(1) Each image was map-projected using a low resolution (10 m) Digital Terrain Model (DTM) covering the area of Beirut to remove the long wavelength stereo component.
(2) Each pair of the tri-stereo image was then automatically correlated to produce a disparity map per pair of images.
(3) Intersection between all the rays coming from the similar points were finally jointly found in the three images to find the high-frequency component of the topography, resulting in a 3D point cloud. The long and short wavelength topography were then added to form the surface elevation at each point in the satellite images.

The point cloud was converted into a grid mesh regularly spaced every 2 m, which is approximately three times the resolution of the initial images. This grid mesh constitutes the Digital Surface Model (DSM) (Fig. 8 (a) and (b)), which represents the elevation model of the earth's surface including the elevation of the above-the-ground features (trees, buildings, etc.). The Digital Features Model (DFM), describing the height of the above-the-ground features- including buildings-, was obtained by subtracting the elevations of the bare earth (DTM) from the DSM as illustrated in Fig. 8 (a) and described below.

[1] https://www.intelligence-airbusds.com/imagery/constellation/pleiades/

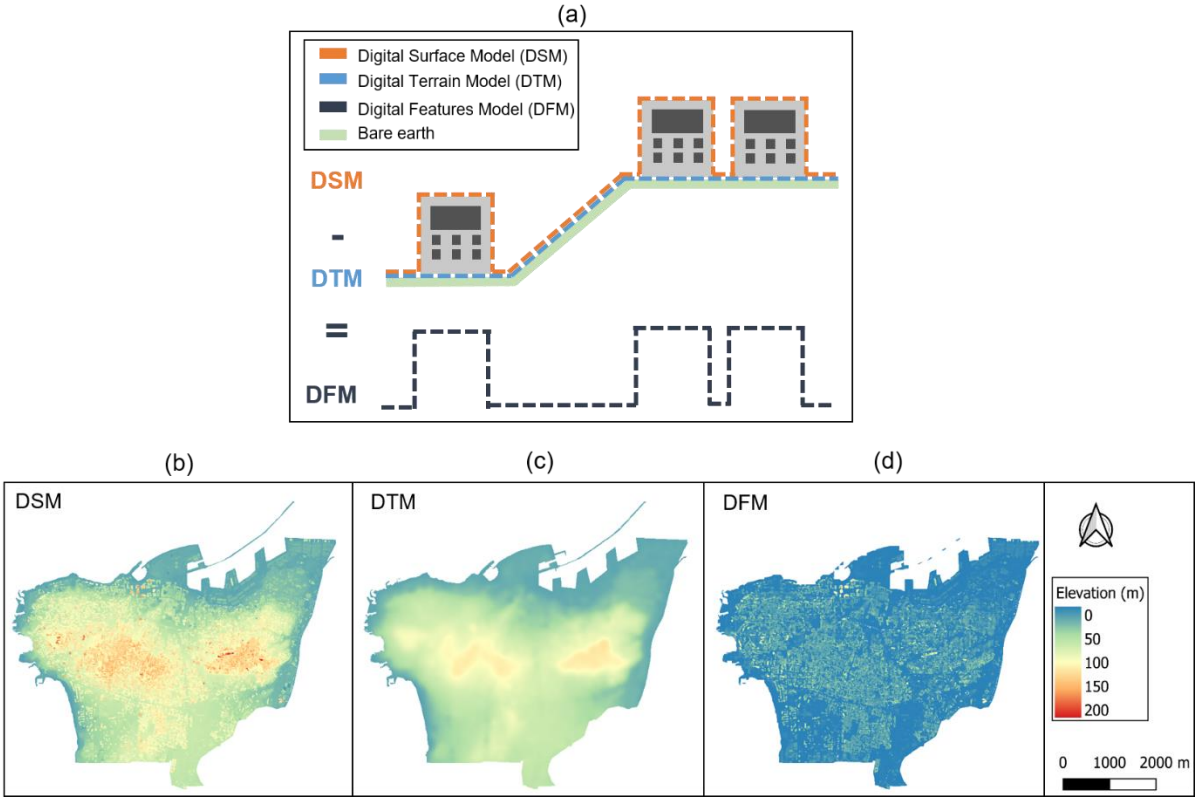

Fig. 8 Digital elevation models derived from processing very high-resolution satellite images. (a) Elevation models processing for obtaining a Digital Features Model from a Digital Surface Model, (b) Digital Surface Model of Beirut, (c) Digital Terrain Model of Beirut, (d) Digital Features Model of Beirut

To derive a high-resolution DTM, the generated DSM was treated in the geographic information system software QGIS (Quantum GIS), using the SAGA-GIS module DTM-filter. This module automatically detects the cells in the DSM corresponding to bare earth and those corresponding to elevated objects. After identifying the bare earth cells, a Digital Terrain Model (DTM) was reconstructed (Fig. 8 (c)) by performing a Multilevel B-spline interpolation in QGIS and filling the gaps between the bare earth cells. The elevations of the DTM were then subtracted from the DSM, which resulted in the generation of a DFM for Beirut (Fig. 8 (d)). Elevations less than 2 m in the DFM were filtered out, since they are too low to correspond to building heights. Then, for each building, the mean DFM value of the cells occupied by the building's footprint was assigned as the building height.

To estimate the error in the prediction of the building's heights from the DFM, we compared the building heights retrieved from the DFM for the LIB-STAT dataset to the heights provided in OSM (when available). When the building height was not indicated in OSM, it was estimated by multiplying the building's number of floors by an approximate story height of 3.5 m. The approximate story height was chosen as 3.5 m because the average story height in Beirut was found to vary between 2.8 m to 4.5 m, depending on the building's construction period (Krayem et al., 2021; Salameh, 2016). On average, the DFM was able to reproduce the building height with a mean error of 14 m (Fig. 9). However, the height of buildings of less than 50 m is slightly overestimated in the

DFM, while the elevation of high-rise buildings (100 m and higher) is mostly underestimated. To investigate the possible causes for this underestimation, we examined the distribution of the DFM values and the quality of the DSM at the location of 9 well-known skyscrapers in Beirut (Table 6 and Fig. 10).

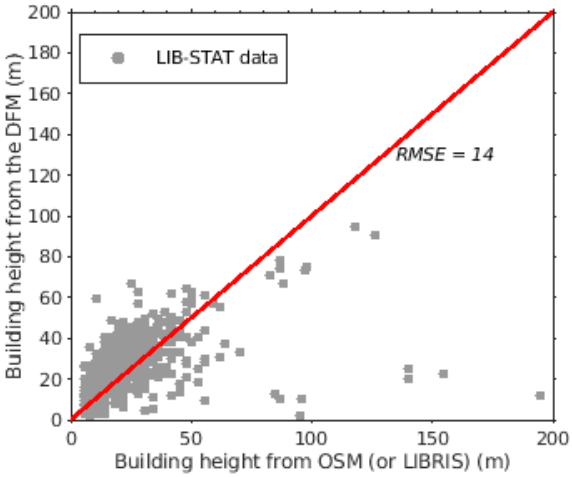

Fig. 9 Comparison of the DFM building heights to the building height retrieved from OSM or from LIBRIS assuming a floor height of 3.5 m

As it appears in Table 6, the highest values taken by the DFM for the "Sama Beirut", "20|30", "Les domes de Sursock" and "Crédit Libanais" towers (35.1 m, 30.8 m, 60.4 m and 27.4 m high, respectively) are significantly lower than the actual building heights which exceed 130 m for the four buildings. Furthermore, the DSM appears to be poorly constrained for these buildings, as the DSM has many "no data" cells (no color) at the buildings' locations (Fig. 10). Moreover, even when DSM data are available, the data are sparse and do not match the building's footprint.

Table 6 Distribution of the DFM values and the quality of the DSM over high-rise buildings in Beirut. The DSM quality is qualified as "poor" when the DSM has many "no data" cells (no color) at the building's location and "OK" otherwise

Building name	**End of construction date**	**Height (from OSM) (m)**	**DFM max. elevation (m)**	**DFM mean elevation (m)**	**DSM quality**
Sama Beirut	2016	195 m	35.1	11.6	Poor
20|30	2016	155 m	30.8	22.4	Poor
Les domes de Sursock	2013	140 m	60.4	25.2	Poor
Crédit Libanais	2015	133 m	27.4	15.1	Poor
Platinum Tower	2008	152 m	141.9	122.6	OK
Marina Tower	2007	150 m	126.7	101.3	OK
Bay Tower	2011	125 m	100.5	107.5	OK
Four Seasons	2009	120 m	121.6	102.7	OK

Beirut Tower	2009	112 m	103.8	95.6	OK

We verified that these buildings already existed at the time when the satellite images were taken (July 2016), as they have all been constructed in 2016 or before. Inversely, the DSM's quality is considerably better for the five other towers, as the DSM has very few no data points at the location of these buildings, and the buildings' footprints can be identified by the higher values taken by the DSM around and under the building footprint. This is also translated by the maximum and mean DFM heights for these buildings, which are close to the actual building heights. Consequently, although the processing of satellite images has shortcomings in the detection of high-rise buildings, the errors are not systematic, as some of the tall buildings in Beirut have been accurately identified. The errors could be due to the buildings' architectural styles, especially the presence of large façade windows possibly influencing the detection of the surface elevation. However, as the errors are not systematic, the heights of buildings retrieved from the satellite images were retained for the subsequent analysis.

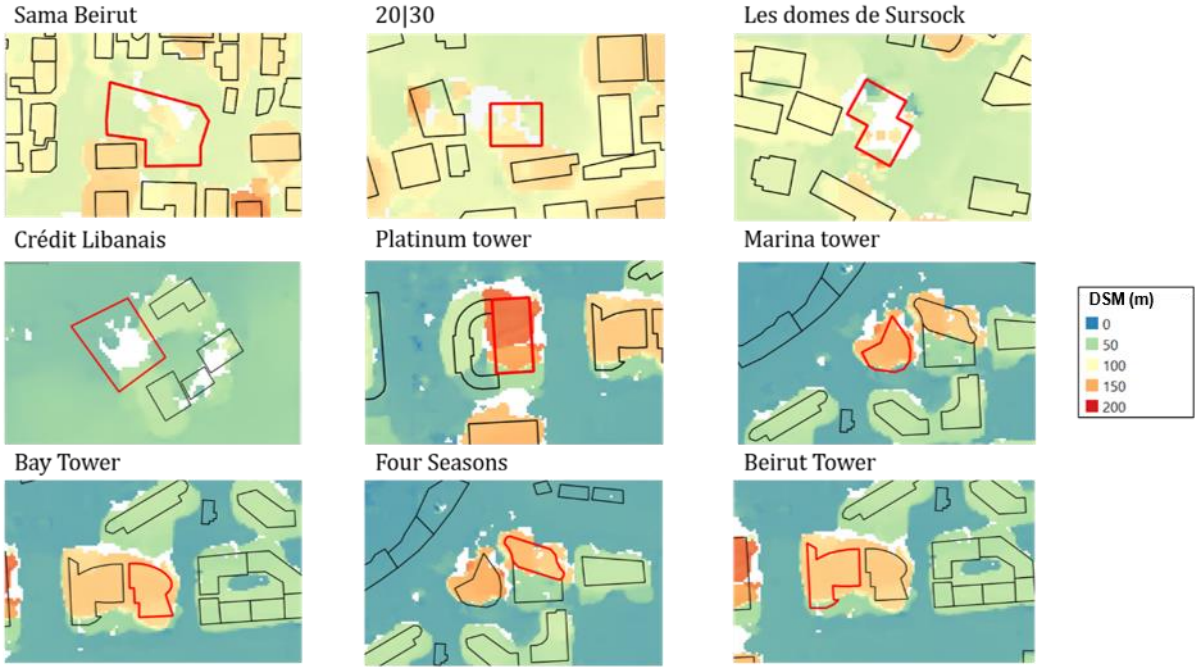

Fig. 10 DSM elevations at the location of 9 high-rise buildings in Beirut. The building's name is indicated on the top the corresponding figure and the corresponding building's footprint is highlighted in red

4.2 Estimation of the buildings' number of floors

The number of floors can be estimated by dividing the building's height by the average story height. As the average story height in Beirut varies according to different sources (Krayem et al., 2021; Salameh, 2016), we relied on a linear regression between the heights of the LIB-STAT buildings retrieved from satellite images and the number of floors of these buildings to derive an empirical story height for buildings in Beirut.

After grouping the LIB-STAT buildings according to their number of floors, we analyzed the distribution of the heights taken by buildings with a similar number of floors (Fig. 11 (a)). For buildings with 2 to 5 floors, the median building height (red line) increases sharply for each additional floor, while the increase is slightly less steep for buildings with 6 or more floors. Buildings with more than 18 floors seem to have unusually low heights, as a consequence of errors in the DFM, and were therefore removed from the regression analysis. A linear regression with no intercept was performed between the number of floors and the heights of the LIB-STAT buildings (Fig. 11 (b)), resulting in an average story height of 3.5 m estimated with a coefficient of determination $R^2 = 0.59$ and a RMSE= 2.47. The RMSE value indicates that the number of floors can be estimated using the linear regression with a mean error of + or – 3 floors. The estimation errors, in terms of the predicted number of floors as a function of the actual number of floors (Fig. 11 (c)) and residuals between the predicted and the actual values Fig. 11 (d), indicate that the number of floors are overestimated for low to medium-rise buildings (10 floors and less), while they are underestimated for buildings higher than 10 floors, as the residuals are mostly negative for these buildings.

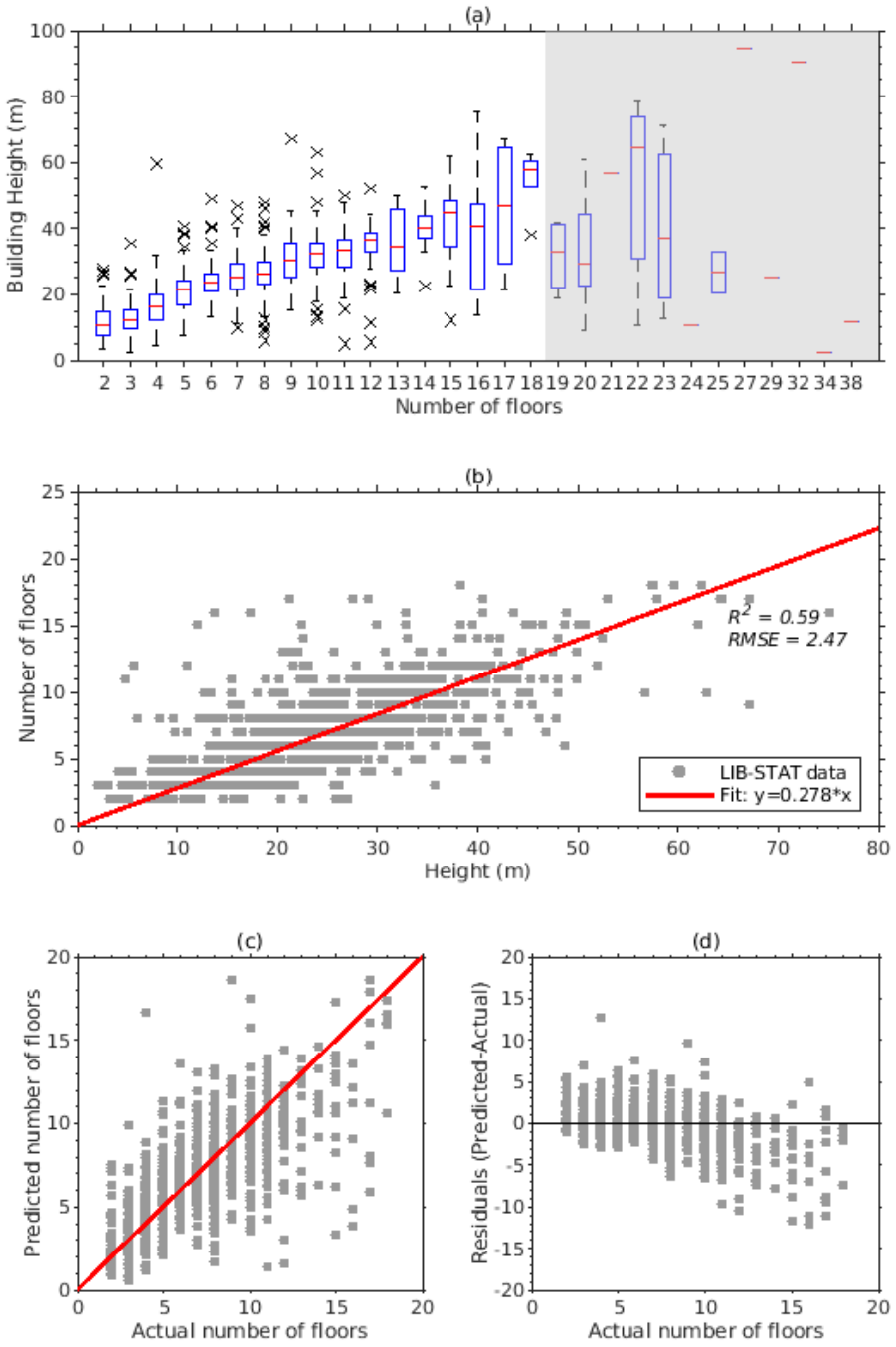

Fig. 11 (a) Boxplot distribution of the building heights according to the number of floors in the LIB-STAT dataset. Outliers are represented by black crosses. (b) Linear regression of the number of floors of the LIB-STAT dataset according to the building heights retrieved from the DFM. Estimation errors (R^2 and RMSE) in the linear regression between the number of floors and the building heights are indicated in the figure. (c) the predicted number of floors as a function of the actual number of floors. (d) the residuals between the predicted and actual value of the number of floors as a function of the actual number of floors

4.3 Prediction of the buildings' construction period

A classification tree is a machine-learning model that can be trained to identify rules for splitting a dataset into subsets based on predictor variables. The resulting model can be applied to classify new datasets. In this paper, we train classification trees on the LIB-STAT dataset to predict the building's construction period based on the available building parameters. First we categorized the construction periods into the 3 classes used for the definition of the building typology: before 1950, between 1950 and 2005 and after 2005. Second, different variables combinations were tested for the choice of predictor variables, namely:

- the building's number of floors, as the height of the building may reflect the evolution of construction materials, building codes and architectural styles over time;
- the building's location (the longitude and latitude coordinates of the building's centroid), which indicates the area in which the building is located and can relate to the evolution of the city's urbanization over time (Yassin, 2012);
- the building's area and perimeter, as the geometrical properties and the size of the building may indicate the evolution of the construction practices over time.

Table 7 The four different classification trees trained and their corresponding performance in terms of validation accuracy

Tree number	Predictors	Validation accuracy
Tree 1	Number of floors	0.7718
Tree 2	Number of floors, Area, Perimeter	0.7583
Tree 3	Number of floors, Longitude, Latitude	0.7958
Tree 4	Number of floors, Longitude, Latitude, Area, Perimeter	0.7838

A classification tree was trained with each set of predictor variables (Table 7). The best accuracy was achieved in Tree 3 where the predictors were the number of floors and the longitude and latitude coordinates of the building. The number of floors was the most important predictor for the construction period, with a weight more than twice as important as the longitude of the building (Fig. 12 (a)). Overall, when comparing the predicted and the true construction period classes (Fig. 12 (b)), buildings built between 1950 and 2005 are over-estimated using the classification tree, while the two other construction periods are underestimated in the predicted sample. This could be explained by the unbalanced input dataset, where the buildings built between 1950 and 2005 are overly represented (Appendix Fig. 24 and Fig. 25) possibly creating a prediction bias and affecting the precision of the classification.

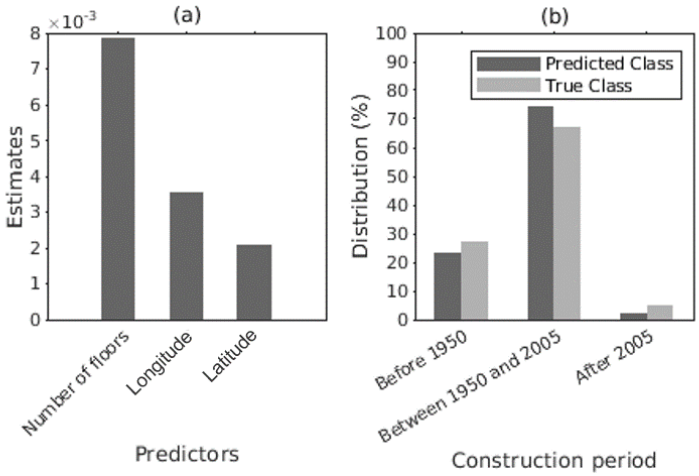

Fig. 12 Prediction of the construction period from the building's number of floors and geographical coordinates using a classification tree. (a) Predictor importance estimates, (b) Distribution of the predicted and true construction periods classes

4.4 Accuracy of the seismic damages estimated with the predicted building characteristics and generation of a complete 3D building model in Beirut

As the main purpose behind the prediction of the building characteristics is to estimate the seismic damages, we assessed the accuracy of the damages inferred from predicted characteristics of the building stock and the damages estimated with the original LIB-STAT dataset's characteristics. The damages were estimated using the ANNs trained in section 2.3 by using the building's resonance frequency and the typology (class) derived from the predicted number of floors and construction period. The detailed comparison of the original and predicted building characteristics can be found in Appendix (Fig. 28). The soil resonance parameters (f_{soil} and A_{0HV}) at the location of each building were extracted as later explained in section 5.1. For a seismic scenario of PGA= 0.3 g and PGV = 16 cm/s as defined in section5, the predicted building characteristics resulted in slightly more severe damage states compared to the original dataset's (Fig. 13 (a)). The percentage of buildings with mean damage values between 1 and 2 decreased from to 71% to 66%, while the percentage of buildings with mean damage values between 2 and 3 increased (from 25% to 31%). The increase of the damage severity could be partially explained by the increase of the percentage of Class 1 buildings (masonry) in the predicted dataset (Appendix Fig. 28). The building-by-building mean damage comparison summarized in the confusion matrix (Fig. 13 (b)), shows that buildings with mean damages between 1 and 2 are predicted with the highest accuracy (73.3%) followed by buildings with mean damages between 2 and 3 (50.6%). Overall, the building mean damages were replicated with an accuracy of 66% at the building-level, which was considered an acceptable trade-off given the reduced size of the training dataset and the limited data available on the buildings in Beirut.

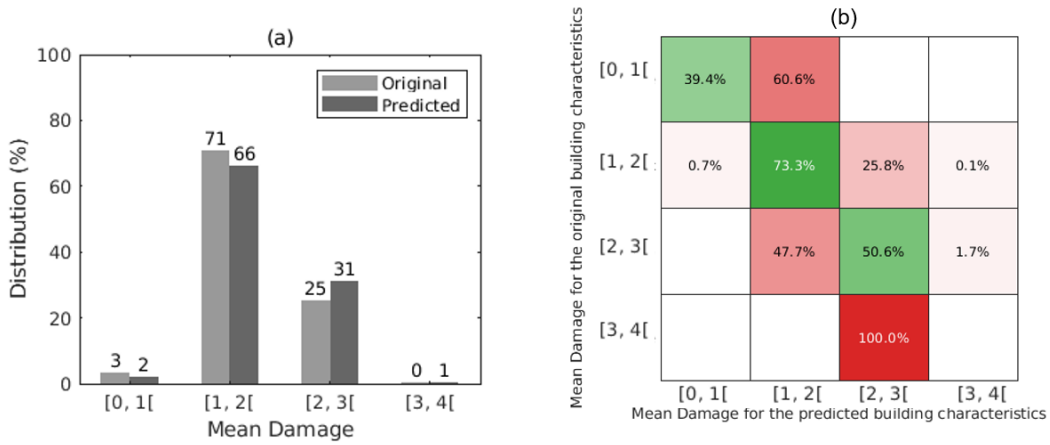

Fig. 13 Comparison of the overall distribution of the building mean damage for the original and predicted characteristics: (a) Distribution of the mean damage of the LIB-STAT dataset for the original and predicted building characteristics, (b) Confusion matrix showing the accuracy of the mean damage estimated at the building-level

After validating the approach on the LIB-STAT dataset, the same steps were followed to retrieve the characteristics of the entire OSM building dataset. This resulted in the characterization of the number of floors, construction period and typology of the 15 089 buildings in Beirut as shown in Fig. 14 and Fig. 15. The generated 3D buildings model in Beirut can be downloaded in the electronic supplement.

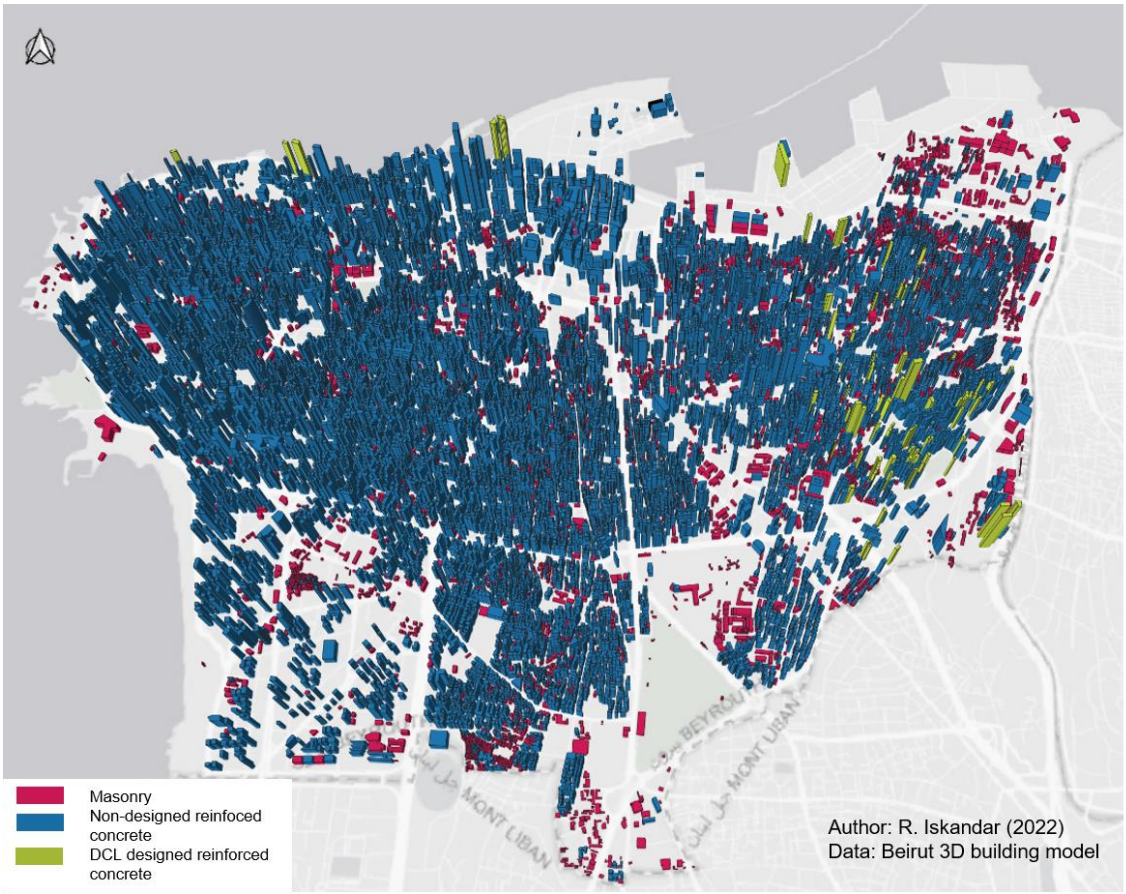

Fig. 14 Generated 3D building model in Beirut with their assigned typology. Buildings in red are masonry buildings (Class 1), buildings in blue are non-designed reinforced concrete (Class 2) and buildings in green are DCL designed reinforced concrete (Class 3).

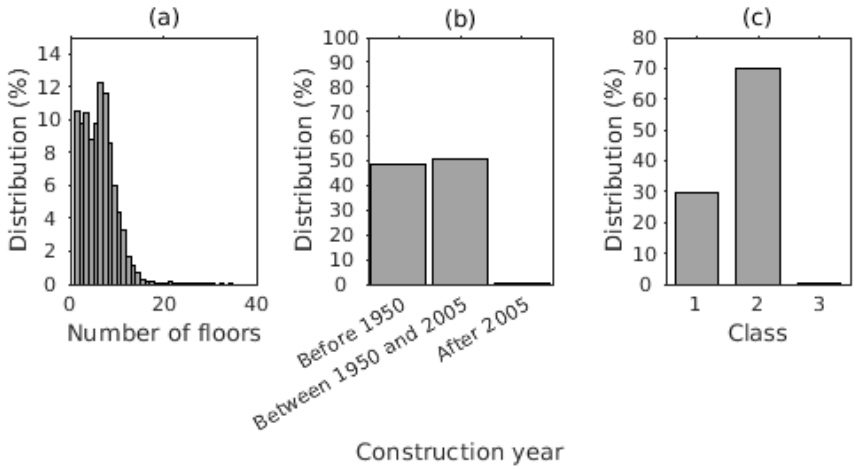

Fig. 15 Distribution of the predicted (a) number of floors, (b) construction year and (c) typology in the generated 3D model of buildings in Beirut

5 Application: estimation of seismic damages and debris at the scale of Beirut

Lebanon is a Middle Eastern country situated on the 1 200 km long Levant Fault System that stretches from the Gulf of Aqaba to Turkey. In Lebanon, the Levant Fault splits into 4 main ramifications: the three left-lateral strike slip faults: the Yammouneh, Roum and Serghaya-Rachaya faults, and the Mount-Lebanon Thrust (Daeron et al., 2007; Elias et al., 2007; Huijer et al., 2016; Walley, 1988). Lebanon and its surroundings have been struck by several strong earthquakes that have caused massive destruction and a high number of fatalities (Khair et al., 2000). The most devastating earthquake in Lebanon was the 551 A.D. earthquake (moment magnitude, M_w ~7.5) attributed to a rupture on the Mount-Lebanon Thrust (Elias et al., 2007). The rupture of the Yammouneh fault in 1202 also caused wide-scale destruction in the Mediterranean region (Daeron et al., 2007; Ellenblum et al., 1998). The double-shock of the 16 March 1956 (M_w = 6.1, M_w = 6.3), was attributed to a rupture on the Roum Fault (Nemer and Meghraoui, 2006) and is the most recent high-magnitude earthquake to affect Lebanon. It killed 136 people, destroyed 6 000 houses and damaged 17 000 others (Harajli et al., 2002). Although Beirut did not witness any major earthquakes in the last couple of decades, the dense urbanization and the only recent and partial implementation of the seismic building code (decrees number 14 293 (2005) and 7 964 (2012)) make the city of Beirut highly vulnerable to earthquakes.

In view of these considerations, scenarios of earthquakes occurring at the Mount Lebanon Thrust (Epicentral distance R = 0 km from Beirut) were considered. The scenarios were fixed based on their PGA value, and their corresponding M_w and PGV values were computed using the ground-motion prediction equation established by Akkar et al. (2014). We defined a first scenario of PGA = 0.3 g, the recommended PGA for the design of earthquake-resistant buildings in Beirut (Huijer et al., 2016). This scenario stands for an earthquake with a M_w of 6.0 on the Mount-Lebanon fault with a PGV of 16 cm/s. Another scenario with a PGA of 0.5 g was also considered. Although pessimistic, this scenario is plausible for near-fault ground motion in Lebanon (Fayjaloun et al., 2021) and corresponds to a M_w of 7.0 and a PGV of 40 cm/s.

5.1 Seismic mean damage estimation in Beirut

The application of the ANNs for the estimation of building mean damages requires soil resonance parameters: f_{soil} and A_{0HV}. Soil investigation campaigns carried out in Beirut and part of it suburbs in the framework of the ANR-LIBRIS project investigated 827 sites using seismic noise recordings (Brax et al., 2018; Salameh et al., 2017; Salloum et al., 2014). The soil fundamental resonance frequency (f_{soil}) was obtained from these recordings using the HVSR (horizontal to vertical spectral ratio) approach (Nakamura, 1989). From these measurements, interpolated maps of both the f_{soil} and A_{0HV} were derived for the surveyed area (Fig. 16 (a) and (b) respectively). The high resonance frequencies (above 10 Hz) and low A_{0HV} (below 1) observed in the east and west of Beirut correspond to outcropping rock. Inversely, the presence of soil deposits can be observed in areas with low resonance frequencies (between 1 and 3 Hz), namely in the northern and the southern parts of Beirut. The soil

resonance parameters: A_{0HV} and f_{soil} at the location of each building were obtained from the interpolated maps in Fig. 16, which also allowed computing f_{struct}/f_{soil} for each building.

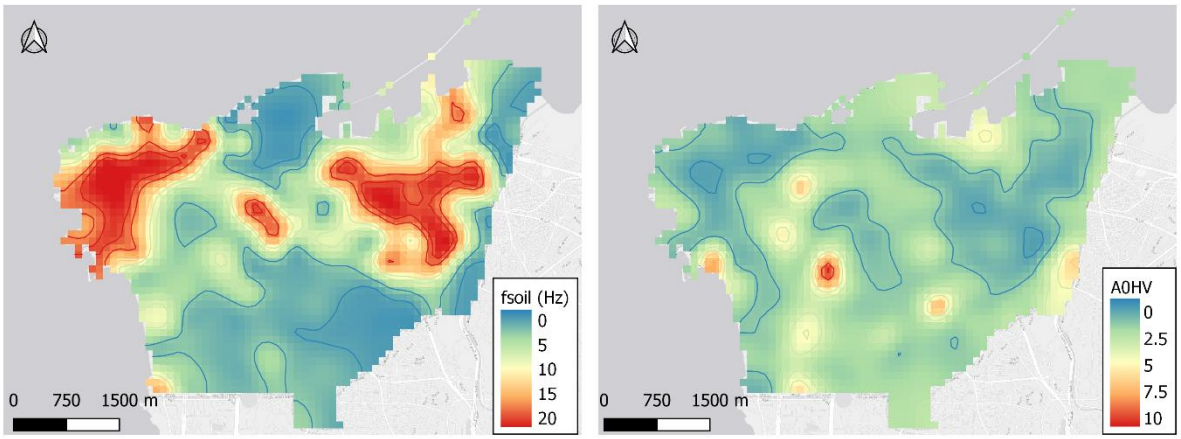

Fig. 16 f_{soil} and A_{0HV} maps in Beirut derived from the cubic-spline interpolation of the ambient vibration measurements performed in Salloum et al. (2014), Salameh et al. (2017) and Brax et al. (2018)

The distribution of the building damage states for the two earthquake scenarios is shown in Table 8 and Table 9. For the earthquake of PGA 0.3 g, most buildings in Beirut are likely to have mean damage between 1 and 2 (60.7% of the buildings) followed by mean damage values between 2 and 3 (33.7%) and mean damage less than 1 (5.5%). 0.1% of the buildings are likely to have a mean damage between 3 and 4, while no buildings are likely to have a mean damage equal to 4. However, it should be noted that although no building reaches a mean damage equal to 4, this does not exclude the possibility of building collapse (see Table 1). For an earthquake of PGA 0.5 g, all buildings in Beirut might have a mean damage greater or equal to 1, 68.1% are likely to have a mean damage between 2 and 3, while 31.4% are likely to have mean damage between 3 and 4. For this scenario too, no buildings are likely to experience a mean damage equal to 4, although some buildings may have collapsed (Table 1).

Table 8 Distribution of the building mean damage for the earthquake scenario of PGA 0.3 g for each building class and for the total number of buildings

Structure	**Mean Damage**				
Type	**[0, 1[**	**[1, 2[**	**[2, 3[**	**[3, 4[**	**4**
Class 1	0	20%	79.6%	0.4%	0
Class 2	7%	78%	15%	0%	0
Class 3	100%	0	0	0	0
All buildings	**5.5%**	**60.7%**	**33.7%**	**0.1%**	**0**

Table 9 Distribution of the building mean damage for the earthquake scenario of PGA 0.5 g for each building class and for the

total number of buildings

Structure	**Mean Damage**				
Type	**[0, 1[**	**[1, 2[**	**[2, 3[**	**[3, 4[**	**4**
Class 1	0	0	89%	11%	0
Class 2	0	0	60%	40%	0
Class 3	0	100%	0	0	0
All buildings	**0**	**0.5%**	**68.1%**	**31.4%**	**0**

Nevertheless, the interpretation of these results should take into account the uncertainty in the predicted building characteristics, especially the error in the building's number of floors that propagates to both the resonance frequency and the typology. To have a first order estimation of the propagation of uncertainty from the number of floors to the mean damages, the latter were also predicted for the mean number of floors (N) plus and minus the standard error of 3 floors (N +3 and N – 3). The related ANNs inputs (f_{struct}/f_{soil} and building typology) were re-computed before estimating the mean damage. As the building's typology depends on the number of floors, the subtraction of 3 floors (N – 3) resulted in an increase in the proportion of Class 1 masonry buildings (Fig. 17 (a)). Contrariwise, the addition of 3 floors (N + 3) led to a slight increase in Class 3 buildings and the disappearance of Class 1, as all buildings would have at least 4 floors. As the buildings' resonance frequency is inversely proportional to the number of floors, the change in the number of floors also translated to an increase of f_{struct}/f_{soil} for N – 3 and a decrease for N + 3 (Fig. 17 (b)).

For scenario 1 (PGA = 0.3 g), the N – 3 configuration led to more pessimistic building damages overall (Fig. 17 (c)). This can be seen by the decrease of the percentage of buildings with mean damage less than 1 and between 1 and 2 from 5% to 2% and from 61% to 47%, respectively, and the increase of the proportion of buildings with mean damage between 2 to 3 from 34% to 50% (Fig. 17 (c)). The opposite trend was observed for the N + 3 configuration (Fig. 17 (c)), as 15% of the buildings had mean damage values less than 1 for this scenario, while the damaged buildings had predominantly mean damage values between 1 and 2 (73%). For scenario 2 (PGA = 0.5 g, Fig. 17 (d)), the percentage of buildings with mean damage between 1 and 2 increased with the increase of the number floors (0 for N – 3, 1% for N and 2% for N + 3). When considering N - 3, the percentage of buildings with mean damage between 2 and 3 increased from 68% to 78%, while the percentage of buildings with mean damage between 3 and 4 decreased from 31% to 22%. Inversely, the addition of 3 floors, resulted in the decrease of the percentage of buildings with mean damage between 2 and 3 (from 68% to 61%) and the increase of the percentage of buildings with mean damage between 3 and 4 (from 31% to 37%). Overall, in scenario 2, as opposed to scenario 1, the decrease of the number of floors resulted in less pessimistic damages, while the increase of number of floors led to more severe damages.

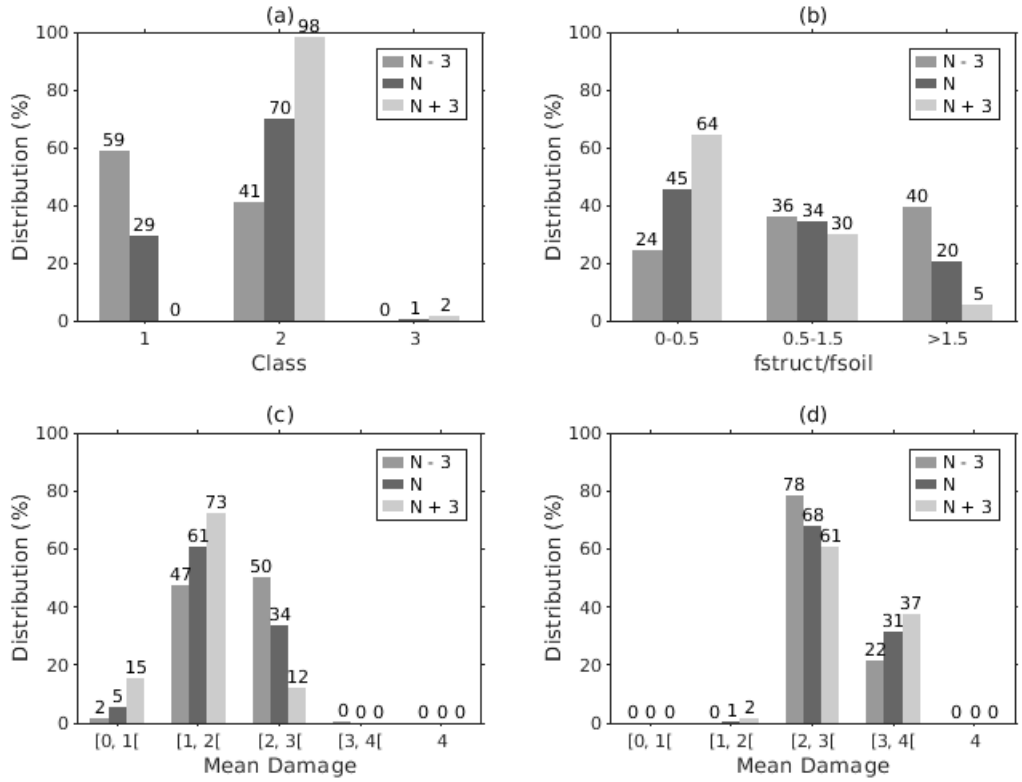

Fig. 17 Variation in the building characteristics and estimated mean damage between the 3 buildings configurations obtained by considering: the mean predicted number of floors (N, dark grey), the mean predicted number of floors -3 (N – 3, grey) and the mean predicted number floors + 3 (N + 3, light grey). (a) Distribution of the building typologies, (b) Distribution of the structure to soil frequency ratio (c) Distribution of the building mean damage for the seismic scenario 1 with PGA = 0.3 g (d) Distribution of the building damage states for the seismic scenario 2 with PGA = 0.5 g

In order to understand the variation of the building damages with the change of number of floors, we analyzed the spatial distribution of the buildings' typology and f_{struct}/f_{soil} for the 3 building configurations (N – 3, N and N + 3) together with the resulting damages for the two seismic scenarios (Fig. 18). Although, the mean damages were computed building by building, for presentation purposes, they were averaged on a radius of 100 m.

For scenario 1, the buildings with the mean number of floors (N) expected to have mean damage between 1 and 2 (Fig. 18 (h)) are concentrated in the east and the west rocky formation of Beirut (Fig. 16). Heavier damages (mean damage between 2 and 3) are concentrated in the north and the south of the city, which are areas prone to site effects (Fig. 16). The spatial distribution of the damages appears to be strongly correlated to the f_{struct}/f_{soil} map in Fig. 18 (e), since higher levels of damages are observed for buildings having f_{struct}/f_{soil} between 0.5 and 1.5 and the lowest building damages are observed when this ratio is less than 0.5 or larger than 1.5. When considering the uncertainty on the number of floors, the building configuration N - 3 suffers overall heavier damages throughout the city (Fig. 18 (g)) compared to building configurations N or N + 3 (Fig. 18 (h) and (i)). Although larger damages (mean damage = 3) are located in narrow regions where f_{struct}/f_{soil} is close to 1, most of the damages (mean damage

= 2) are caused by more vulnerable buildings (most of the buildings are Class 1, Fig. 18 (a)) located on sites exhibiting site effects, and thus subject to larger surface ground motion for which the Class 1 buildings are especially sensitive to (Fig. 2). The control of the coincidence of frequencies between soils and buildings on the spatial distribution of the building damages is remarkable when considering the building configuration N + 3 (Fig. 18 (f) and (i)), since most buildings at sediment sites exhibit a f_{struct}/f_{soil} close to 1 (Fig. 18 (f)).

In scenario 2, most buildings suffer heavy damages (mean damage > 3) regardless of the building's number of floors (Fig. 18 (j) (k) and (l)). Nevertheless, the building damages are less severe at rock sites (mostly mean damage = 3 whatever the building's number of floors) in the east and the west of Beirut compared to the north and south sediment sites. Interestingly, less severe damages are observed at sediment sites for the building configuration N - 3 compared to N and N + 3. This can be explained by the reduction of the soil's amplification at the building resonance frequency due to the nonlinearity of the soil response. Since most of the N - 3 building resonance frequencies correspond to f_{struct}/f_{soil} larger than 1.5 at sediment sites, this ratio is even increased when considering the decrease of soil's resonance frequency due to non-linearity in conjunction also with a decrease of seismic motion beyond f_{soil}, leading to less severe damage levels. For the N + 3 configuration, most of the f_{struct}/f_{soil} range from 0.5 to 1.5 at sediment sites (Fig. 18 (f)). When f_{soil} decreases due to the soil's non-linear behavior, buildings with f_{struct}/f_{soil} between 0.5 and 1 will be more prone to more structural displacement because of the coincidence of resonance frequencies.

Despite the differences observed in the distribution of the damage severity when considering the uncertainty in the building properties, the spatial distribution of the damages exhibits heavier building damages at sediment sites in the north and the south of Beirut, while the buildings located on the rock sites in the east and the west of Beirut are expected to witness the lowest levels of damages. These observations confirm that the site effects and the coincidence of frequencies between soils and buildings control on the first order the spatial distribution of damages, while the building's configuration (i.e. relative distribution between the buildings' vulnerability classes) controls the severity of the expected damages.

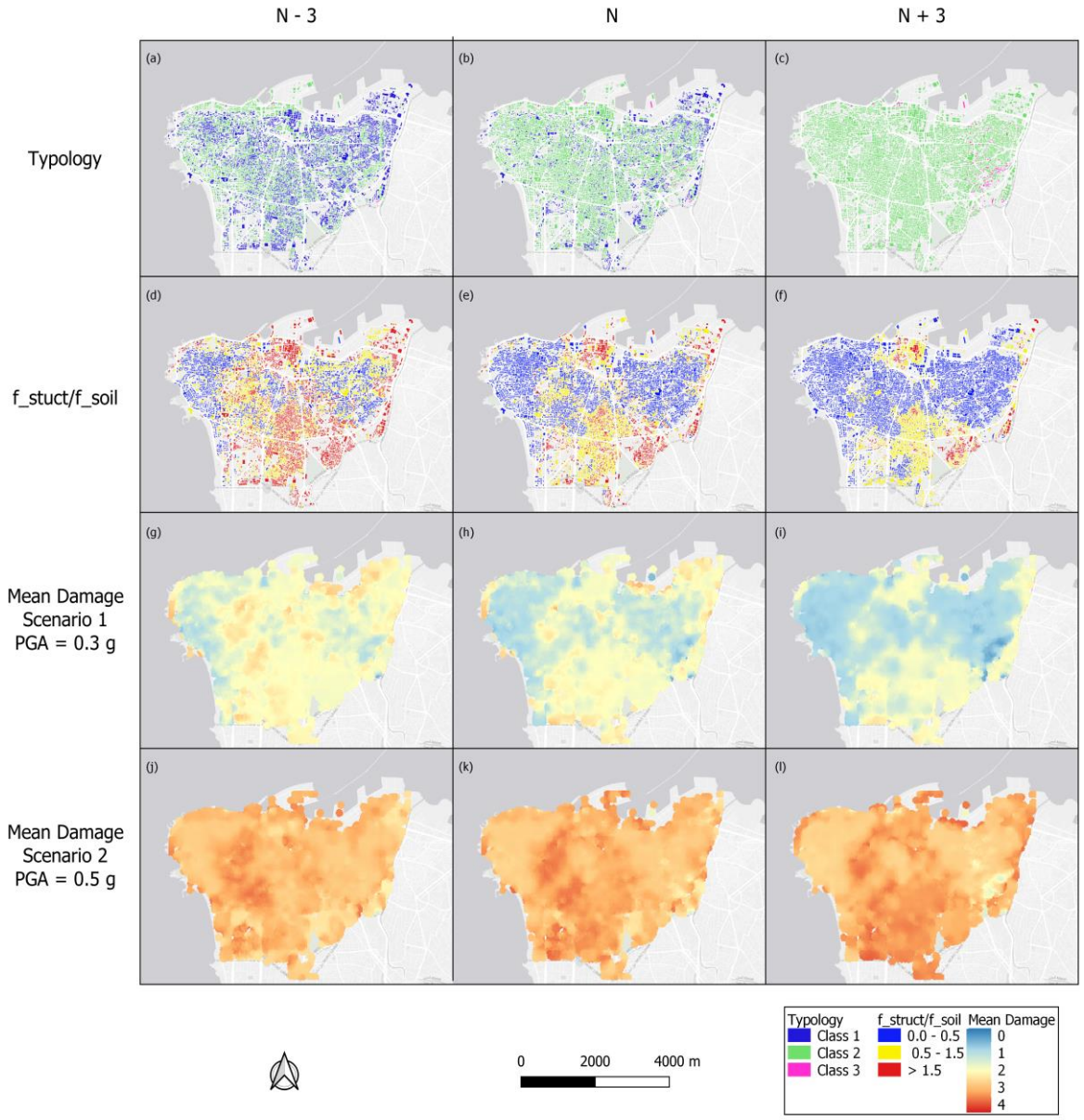

Fig. 18 Beirut mean damage maps for various buildings configurations with the average predicted number of floors -3 (N-3, a and d), predicted number of floors (N, b and e) and predicted number of floors +3 (N+3, c and f) for scenario 1 (g, h and i) and scenario 2 (j, k and l). The mean damages (g to l) were computed building by building, but for presentation purposes they were averaged on a radius of 100 m

5.2 Debris estimation

The extent and height of debris in Beirut were estimated for the two earthquakes scenarios for the building configuration with the average predicted number of floors (N). The debris extents vary according to the building's height and mean damage (Fig. 19). For a given building height or mean damage, the debris extent increases with increasing building damages or building height. For the scenario with a PGA of 0.3 g, debris are expected to reach

up to 1.8 m away from buildings in Beirut (Fig. 19 (a)). The limited debris extent in this scenario can be attributed to the fact that masonry buildings, which are more prone to significant damage and generate more debris, are limited to a maximum height of four stories. Whereas taller buildings are more likely to be of reinforced concrete, resulting in a smaller amount of debris being generated. In contrast, for the scenario with PGA of 0.5 g (Fig. 19 (b)), as the buildings experience greater damages, the extent of debris around buildings are significantly larger than in the first scenario, reaching up to 6.5 m for heavily damaged tall buildings.

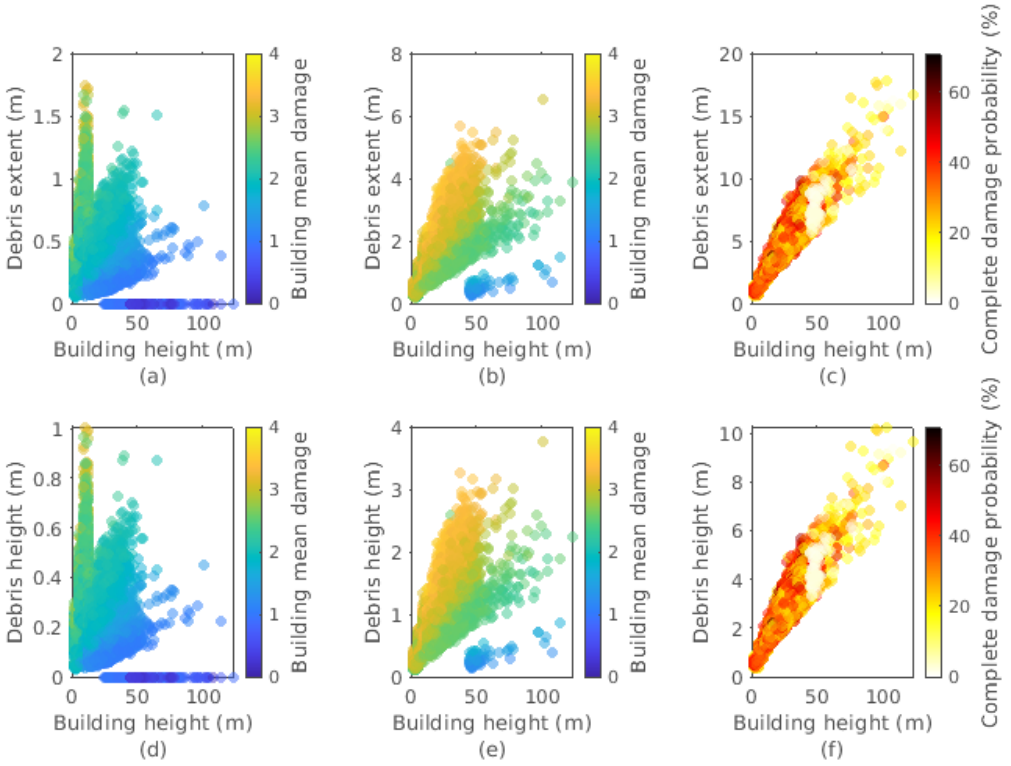

Fig. 19 Distribution of the debris extent and height according to the building height and the mean damage. Debris extent for (a) Seismic scenario of PGA = 0.3 g, (b) Seismic scenario of PGA = 0.5 g and (c) in case complete damage for a seismic scenario of PGA = 0.5 g with the associated probability of occurrence. Debris height for (d) Seismic scenario of PGA = 0.3 g, (e) Seismic scenario of PGA = 0.5 g and (f) in case complete damage for a seismic scenario of PGA = 0.5 g with the associated probability of occurrence

As the debris height is also important for urban mobility in the aftermath of an earthquake, we have examined the distribution of debris heights for the two seismic scenarios. The debris height follows exactly the same distribution as the debris extents in the two scenarios: with increasing building heights and damage levels, the debris heights increase as well. While the maximum debris height in the scenario with PGA= 0.3 g (Fig. 19 (d)) is of 1 m, in scenario with PGA= 0.5 g (Fig. 19 (e)) the debris are considerably higher, reaching up to 3.8 m in the case of heavily damaged tall buildings. Debris are expected to reach heights greater than 1 m, particularly in the Mazraa and Moussaitbeh sectors (Fig. **20**). The heights of debris in these areas should be taken into account by emergency management planners due to the increased mobility challenges to pedestrian and vehicles caused by the presence

of debris.

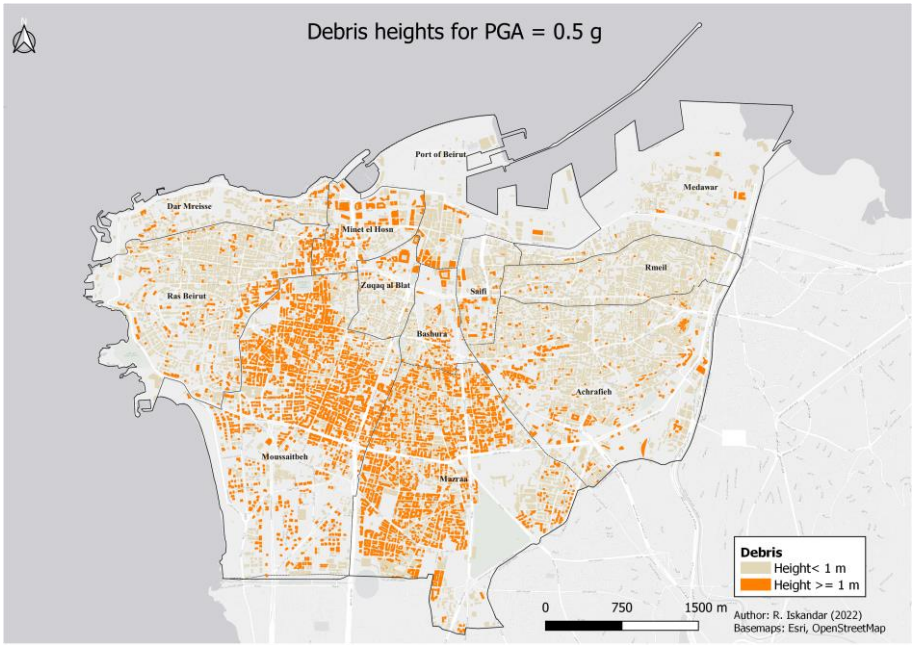

Fig. 20 Spatial distribution of the debris heights in Beirut for a seismic scenario of PGA = 0.5 g

However, it should be noted that the debris estimated herein corresponds to the most probable damage state based on the mean damage value (see Table 4 and Table 5). This does not exclude the possibility of experiencing wider and higher debris, especially in the case of complete building damage. To illustrate the maximum debris that can be expected for the more pessimistic scenario of PGA 0.5 g, we have computed the debris extent and height for each building in case of complete damage, along with the corresponding probability of complete damage (Fig. 19 (c) and (f)). For this earthquake scenario, the debris can reach up to 18 m away from buildings and up to 10 m high with a probability of occurrence around 20%. However, for certain buildings, the likelihood of debris reaching up to 10 m away from buildings and a height of 6 m rises significantly to 70%.

6 Conclusion

This paper proposes methodological improvements to estimate seismic damages and debris in urban areas from building-level simulations, along with the generation of a complete 3D building model for the city of Beirut (Lebanon) and the characterization of its vulnerability based on open-source geographic data, very high-resolution satellite images and machine learning tools. Artificial Neural Networks (ANNs) were trained to predict buildings mean damages computed from extensive simulations of site and building responses to synthetic input motions. Several proxies for building, soil and input seismic motion properties were tested to find the optimal predictors of the mean damage. Although PGV was found to be a better proxy for the input ground motion than the PGA, better damage prediction performances were achieved by considering both the PGA and the PGV simultaneously. Regarding the proxies related to soil and building properties, the frequency ratio f_{struct}/f_{soil} explained better the

damage for reinforced concrete buildings (Classes 2 and 3), while considering f_{struct} and f_{soil} separately improved the prediction of mean damages in masonry buildings (Class 1). A_{0HV} performed better than f_{soil} in the damage prediction when considered with f_{struct}/f_{soil}. Nevertheless, the best performances were obtained when considering PGA, PGV, A_{0HV} and f_{struct}/f_{soil} as input variables in the ANNs. The corresponding ANNs for each building class were derived for the estimation of the building mean damages in urban areas. The proposed methodology for the estimation of damaged-induced debris provides the height and extent of debris around buildings, while considering the level of building damage. The volume of generated debris in the case of full collapse is estimated first. Then, using correlations between the building's damage and the generated debris quantity, the debris volume corresponding to the building's damage level is estimated and distributed around the building. This methodology was validated by comparing its results to usual values found in the literature for full collapse buildings. Although the calibration of the model should be improved for high-rise buildings, it showed good results for low-to-moderate rise buildings. A complete 3D building model was developed for the city of Beirut in Lebanon. Building footprints were collected from the volunteered geographic information database, OSM, and the height of these buildings was retrieved from the analysis of very high-resolution Pleaides 1-B satellite images. A subset of around 1000 buildings with known attributes, taken from an existing building dataset, was used to derive statistical relationships between different building attributes (building height, number of floors, resonance frequency, typology) in order to extrapolate the building properties at the city scale.

The proposed methodologies were applied to estimate the seismic damages and debris in Beirut for two earthquake scenarios corresponding to PGA of 0.3 g and 0.5 g. The damages predicted at the building scale indicate that the damages are concentrated in sediment areas, larger damages occurring when the ratio between soil and building resonance frequency is close to 1 (double resonance phenomenon), while the damage levels depend on the seismic scenario considered. Although for the scenario with PGA = 0.3 g the debris extent and height are relatively low (maximum debris extent 1.8 m and maximum height 1 m), for the scenario with PGA = 0.5 g the debris reach further around buildings (up to 6.5 m) and have heights of over 1 m that could severely constrain post-seismic mobility. Nevertheless, as in any estimation, there is an uncertainty in the estimated damages and debris. One of the uncertainty factors comes from the difficulty in accurately quantifying the buildings' heights from satellite images, which in turn influences the number of floors and other building attributes such as the building's resonance frequency and its typology. The effect of the uncertainty in the estimated number of floors on the predicted damages was explored by comparing the damages estimated for the average predicted number of floors and the damages computed for the average number of floors plus and minus the standard error of 3 floors. The changes in the number of floors translate into a possible change of building vulnerability class and an increase or decrease of f_{stuct}/f_{soil}. While the overall distribution of damage states varies depending on the building configuration, the spatial distribution of the damages throughout the city is consistent with the damage distribution for the average predicted number of floors. This highlights the control of the site effects on the buildings damages, as despite the variability of the building properties, the damages were still concentrated in the same areas in the city. Therefore, although the generated 3D building model does not substitute a complete and detailed buildings exposure model, it can provide a starting point for the analysis of the distribution of seismic damages and debris within urban areas. The

approach developed in this study, which relies on simple measure parameters, may be particularly useful in other cities with a similar context to Beirut, where comprehensive building data stock is lacking.

In future works we plan to complement this study with a more comprehensive analysis of the propagation of uncertainty from the estimated building parameters to the building damages. Furthermore, the shortcomings found in the estimation of the elevation of high-rise buildings using satellite images will be further investigated to identify their possible reasons and improve the characterization of the building heights. Additionally, one of the limitations of our study is related to the use of HAZUS to estimate the debris quantity, while HAZUS is primarily calibrated for the United States where buildings differ in quality and type compared to those in Lebanon. The debris estimation model could be improved by calibrating it in an experimental setup, such as performing experiments on a shaking table and observing the extent and height of the generated debris. Finally, the experiments can be validated by observations from real events through the analysis of satellite images and street-view photography in pre/post-earthquake conditions, eventually combined with in-situ evaluation of building typologies. This would allow establishing empirical relationships between the ground motion, the building typology and the generated debris.

References

Agence nationale de la recherche, 2010. LIBRIS [WWW Document]. URL https://anr.fr/Projet-ANR-09-RISK-0006 (accessed 5.11.23).

Akkar, S., Sandıkkaya, M.A., Bommer, J.J., 2014. Empirical ground-motion models for point- and extended-source crustal earthquake scenarios in Europe and the Middle East. Bull Earthquake Eng 12, 359–387. https://doi.org/10.1007/s10518-013-9461-4

Argyroudis, S., Selva, J., Gehl, P., Pitilakis, K., 2015. Systemic Seismic Risk Assessment of Road Networks Considering Interactions with the Built Environment: Systemic seismic risk assessment of road networks. Computer-Aided Civil and Infrastructure Engineering 30, 524–540. https://doi.org/10.1111/mice.12136

Assimaki, D., Li, W., Kalos, A., 2011. A Wavelet-based Seismogram Inversion Algorithm for the In Situ Characterization of Nonlinear Soil Behavior. Pure Appl. Geophys. 168, 1669–1691. https://doi.org/10.1007/s00024-010-0198-6

Beresnev, I.A., Wen, K.-L., 1996. Nonlinear soil response—A reality? Bulletin of the Seismological Society of America 86, 1964–1978.

Bonilla, L., 2005. Hysteretic and Dilatant Behavior of Cohesionless Soils and Their Effects on Nonlinear Site Response: Field Data Observations and Modeling. The Bulletin of the Seismological Society of America 95, 2373–2395. https://doi.org/10.1785/0120040128

Bonilla, L.F., 2001. NOAH: users manual. Institute for Crustal Studies, University of California, Santa Barbara 38.

Borcherdt, R.D., 1970. Effects of local geology on ground motion near San Francisco Bay. Bulletin of the Seismological Society of America 60, 29–61.

Braga, F., Dolce, M., Liberatore, D., 1982. A statistical study on damaged buildings and an ensuing review of the MSK-76 scale, in: Proceedings of the Seventh European Conference on Earthquake Engineering, Athens, Greece. pp. 431–450.

Brax, M., Bard, P.-Y., Duval, A.-M., Bertrand, E., Rahhal, M.-E., Jomaa, R., Cornou, C., Voisin, C., Sursock, A., 2018. Towards a microzonation of the Greater Beirut area: an instrumental approach combining earthquake and ambient vibration recordings. Bulletin of Earthquake Engineering 16, 5735–5767. https://doi.org/10.1007/s10518-018-0438-1

Broxton, M.J., Edwards, L.J., 2008. The Ames Stereo Pipeline: Automated 3D Surface Reconstruction from Orbital Imagery. Presented at the 39th Lunar and Planetary Science Conference, (Lunar and Planetary Science XXXIX), League City, Texas.

Calvi, G.M., Pinho, R., Magenes, G., Bommer, J.J., Restrepo-Vélez, L.F., Crowley, H., 2006. Development of seismic vulnerability assessment methodologies over the past 30 years. ISET Journal of Earthquake Technology 43, 75–104.

Castro, S., Poulos, A., Herrera, J.C., de la Llera, J.C., 2019. Modeling the Impact of Earthquake-Induced Debris on Tsunami Evacuation Times of Coastal Cities. Earthquake Spectra 35, 137–158. https://doi.org/10.1193/101917EQS218M

Cetin, K.O., Altun, S., Askan, A., Akgün, M., Sezer, A., Kıncal, C., Özdağ, Ö.C., İpek, Y., Unutmaz, B., Gülerce, Z., Özacar, A.A., Ilgaç, M., Can, G., Cakir, E., Söylemez, B., El-Sayeed, A., Zarzour, M., Bozyiğit, İ., Tuna, Ç., Köksal, D., Karimzadeh, S., Uzel, B., Karaali, E., 2022. The site effects in Izmir Bay of October 30 2020, M7.0 Samos Earthquake. Soil Dynamics and Earthquake Engineering 152, 107051. https://doi.org/10.1016/j.soildyn.2021.107051

Chopra, A.K., Goel, R.K., 1999. Capacity-Demand-Diagram Methods Based on Inelastic Design Spectrum. Earthquake Spectra 15, 637–656. https://doi.org/10.1193/1.1586065

Crowley, H., Despotaki, V., Rodrigues, D., Silva, V., Toma-Danila, D., Riga, E., Karatzetzou, A., Fotopoulou, S., Zugic, Z., Sousa, L., Ozcebe, S., Gamba, P., 2020. Exposure model for European seismic risk assessment. Earthquake Spectra 36, 252–273. https://doi.org/10.1177/8755293020919429

Daeron, M., Klinger, Y., Tapponnier, P., Elias, A., Jacques, E., Sursock, A., 2007. 12,000-Year-Long Record of 10 to 13 Paleoearthquakes on the Yammouneh Fault, Levant Fault System, Lebanon. Bulletin of the Seismological Society of America 97, 749–771. https://doi.org/10.1785/0120060106

Darendeli, M.B., 2001. Development of a New Family of Normalized Modulus Reduction and Material Damping Curves. University of Texas, Austin.

Domaneschi, M., Cimellaro, G.P., Scutiero, G., 2019. A simplified method to assess generation of seismic debris for masonry structures. Engineering Structures 186, 306–320. https://doi.org/10.1016/j.engstruct.2019.01.092

Dubertret, L., 1945. Géologie du Site de Beyrouth avec carte geologique 1/20,000, in: Delegation Generale de France Au Levant, Section Geologique; pp. 1–5.

Elias, A., Tapponnier, P., Singh, S.C., King, G.C.P., Briais, A., Daëron, M., Carton, H., Sursock, A., Jacques, E.,

Jomaa, R., Klinger, Y., 2007. Active thrusting offshore Mount Lebanon: Source of the tsunamigenic A.D. 551 Beirut-Tripoli earthquake. Geology 35, 755–758. https://doi.org/10.1130/G23631A.1

Ellenblum, R., Marco, S., Agnon, A., Rockwell, T., Boas, A., 1998. Crusader castle torn apart by earthquake at dawn, 20 May 1202. Geol 26, 303. https://doi.org/10.1130/0091-7613(1998)026<0303:CCTABE>2.3.CO;2

Elnashai, A.S., Di Sarno, L., 2008. Fundamentals of earthquake engineering. Wiley New York.

Fayjaloun, R., Dabaghi, M., Cornou, C., Causse, M., Lu, Y., Stehly, L., Voisin, C., Mariscal, A., 2021. Hybrid Simulation of Near-Fault Ground Motion for a Potential Mw 7 Earthquake in Lebanon. Bulletin of the Seismological Society of America. https://doi.org/10.1785/0120210091

Federal Emergency Management Agency (FEMA), 2012. Multi-hazard loss estimation methodology, earthquake model HAZUS-MH 2.1 technical manual. Federal Emergency Management Agency, Washington, DC, United States.

Finn, W.D.L., 1991. Geotechnical engineering aspects of microzonation. Presented at the Fourth International Conference on Seismic Zonation, Stanford, California, pp. 236–253.

Frankel, A., 2002. Nonlinear and Linear Site Response and Basin Effects in Seattle for the M 6.8 Nisqually, Washington, Earthquake. Bulletin of The Seismological Society of America - BULL SEISMOL SOC AMER 92, 2090–2109. https://doi.org/10.1785/0120010254

Freeman, S.A., Associates, E., Street, P., 2004. Review of the development of the capacity spectrum method. ISET Journal of Earthquake Technology 41, 1–13.

Gehl, P., Auclair, S., Fayjaloun, R., Meresse, P., 2022. Decision support for emergency road traffic management in post-earthquake conditions. International Journal of Disaster Risk Reduction 103098. https://doi.org/10.1016/j.ijdrr.2022.103098

Geiß, C., Schauß, A., Riedlinger, T., Dech, S., Zelaya, C., Guzmán, N., Hube, M., Jokar Arsanjani, J., Taubenböck, H., 2017. Joint use of remote sensing data and volunteered geographic information for exposure estimation: evidence from Valparaíso, Chile. Natural Hazards 86. https://doi.org/10.1007/s11069-016-2663-8

Gomez-Zapata, J., Zafrir, R., Pittore, M., Merino, Y., 2022. Towards a Sensitivity Analysis in Seismic Risk with Probabilistic Building Exposure Models: An Application in Valparaíso, Chile Using Ancillary Open-Source Data and Parametric Ground Motions. ISPRS International Journal of Geo-Information 11, 113. https://doi.org/10.3390/ijgi11020113

Grünthal, G., 1998. European macroseismic scale 1998 : EMS-98, Cahiers du Centre Européen de Géodynamique et de Séismologie. Ministère de la culture, de l'enseignement supérieur et de la recherche, Luxembourg.

Harajli, M., Sadek, S., Asbahan, R., 2002. Evaluation of the seismic hazard of Lebanon. Journal of Seismology 6, 257–277.

Hardin, B.O., Drnevich, V.P., 1972a. Shear Modulus and Damping in Soils: Measurement and Parameter Effects (Terzaghi Leture). J. Soil Mech. and Found. Div. 98, 603–624. https://doi.org/10.1061/JSFEAQ.0001756

Hardin, B.O., Drnevich, V.P., 1972b. Shear Modulus and Damping in Soils: Design Equations and Curves. J. Soil

Mech. and Found. Div. 98, 667–692. https://doi.org/10.1061/JSFEAQ.0001760

Huijer, C., Harajli, M., Sadek, S., 2016. Re-evaluation and updating of the seismic hazard of Lebanon. J Seismol 20, 233–250. https://doi.org/10.1007/s10950-015-9522-z

Kaklamanos, J., Baise, L.G., Thompson, E.M., Dorfmann, L., 2015. Comparison of 1D linear, equivalent-linear, and nonlinear site response models at six KiK-net validation sites. Soil Dynamics and Earthquake Engineering 69, 207–219.

Kästli, P., Fäh, D., 2006. Rapid estimation of macroseismic effects and shake maps combining macroseismic and instrumental data. Presented at the Proceedings of the First European Conference on Earthquake Engineering and Seismology (ECEES), Geneva, Switzerland.

Khair, K., Karakaisis, G.F., Papadimitriou, E., 2000. Seismic zonation of the Dead Sea Transform Fault area. Annals of Geophysics 43.

Kim, B., Hashash, Y.M., Stewart, J.P., Rathje, E.M., Harmon, J.A., Musgrove, M.I., Campbell, K.W., Silva, W.J., 2016. Relative differences between nonlinear and equivalent-linear 1-D site response analyses. Earthquake Spectra 32, 1845–1865.

Kramer, S.L., 1996. Geotechnical earthquake engineering. Pearson Education India.

Krayem, A., Yeretzian, A., Faour, G., Najem, S., 2021. Machine learning for buildings' characterization and power-law recovery of urban metrics. PLoS ONE 16, e0246096. https://doi.org/10.1371/journal.pone.0246096

Lacroix, P., 2016. Landslides triggered by the Gorkha earthquake in the Langtang valley, volumes and initiation processes. Earth Planets Space 68, 46. https://doi.org/10.1186/s40623-016-0423-3

Lagomarsino, S., Giovinazzi, S., 2006. Macroseismic and mechanical models for the vulnerability and damage assessment of current buildings. Bulletin of Earthquake Engineering 4, 415–443. https://doi.org/10.1007/s10518-006-9024-z

Lantada, N., Irizarry, J., Barbat, A.H., Goula, X., Roca, A., Susagna, T., Pujades, L.G., 2010. Seismic hazard and risk scenarios for Barcelona, Spain, using the Risk-UE vulnerability index method. Bulletin of Earthquake Engineering 8, 201–229. https://doi.org/10.1007/s10518-009-9148-z

Lantada, N., Pujades, L.G., Barbat, A.H., 2009. Vulnerability index and capacity spectrum based methods for urban seismic risk evaluation. A comparison. Natural Hazards 51, 501–524. https://doi.org/10.1007/s11069-007-9212-4

Liuzzi, M., Aravena Pelizari, P., Geiß, C., Masi, A., Tramutoli, V., Taubenböck, H., 2019. A transferable remote sensing approach to classify building structural types for seismic risk analyses: the case of Val d'Agri area (Italy). Bull Earthquake Eng 17, 4825–4853. https://doi.org/10.1007/s10518-019-00648-7

Lu, X., Yang, Z., Cimellaro, G.P., Xu, Z., 2019. Pedestrian evacuation simulation under the scenario with earthquake-induced falling debris. Safety Science 114, 61–71. https://doi.org/10.1016/j.ssci.2018.12.028

Luzi, L., Puglia, R., Pacor, F., Gallipoli, M., Bindi, D., Mucciarelli, M., 2011. Proposal for a soil classification based on parameters alternative or complementary to Vs,30. Bulletin of Earthquake Engineering - BULL EARTHQ ENG 9. https://doi.org/10.1007/s10518-011-9274-2

Mayoral, J., Asimaki, D., Tepalcapa, S., Wood, C., Román-de la Sancha, A., Hutchinson, T., Franke, K., Montalva, G., 2019. Site effects in Mexico City basin: Past and present. Soil Dynamics and Earthquake Engineering 121, 369–382. https://doi.org/10.1016/j.soildyn.2019.02.028

McCulloch, W.S., Pitts, W., 1943. A logical calculus of the ideas immanent in nervous activity. The bulletin of mathematical biophysics 5, 115–133.

Mesta, C., Santa-Cruz, S., Kahhat, R., 2020. Probabilistic assessment of earthquake-induced debris generation using pbee methodology. Presented at the 17th World Conference on earthquake engineering, 17WCEE, Sendai, Japan.

Minsky, M., Papert, S., 1969. An introduction to computational geometry. Cambridge tiass., HIT 479, 480.

Mouroux, P., Le Brun, B., 2006. Risk-Ue Project: An Advanced Approach to Earthquake Risk Scenarios With Application to Different European Towns, in: Assessing and Managing Earthquake Risk. Geotechnical, Geological And Earthquake Engineering. Springer, Dordrecht, pp. 479–508.

Nakamura, Y., 1989. A method for dynamic characteristics estimation of subsurface using microtremor on the ground surface. Railway Technical Research Institute, Quarterly Reports 30.

National Research Institute for Earth Science and Disaster Resilience, 2019. K-NET, KiK-net, National Research Institute for Earth Science and Disaster Resilience.

Nemer, T., Meghraoui, M., 2006. Evidence of coseismic ruptures along the Roum fault (Lebanon): a possible source for the AD 1837 earthquake. Journal of Structural Geology 28, 1483–1495. https://doi.org/10.1016/j.jsg.2006.03.038

Nievas, C.I., Pilz, M., Prehn, K., Schorlemmer, D., Weatherill, G., Cotton, F., 2022. Calculating earthquake damage building by building: the case of the city of Cologne, Germany. Bull Earthquake Eng 20, 1519–1565. https://doi.org/10.1007/s10518-021-01303-w

Nishino, T., Tanaka, T., Hokugo, A., 2012. An evaluation method for the urban post-earthquake fire risk considering multiple scenarios of fire spread and evacuation. Fire Safety Journal 54, 167–180. https://doi.org/10.1016/j.firesaf.2012.06.002

OpenStreetMap [WWW Document], 2023. . OpenStreetMap. URL https://www.openstreetmap.org/ (accessed 5.11.23).

Peek-Asa, C., 2003. Seismic, structural, and individual factors associated with earthquake related injury. Injury Prevention 9, 62–66. https://doi.org/10.1136/ip.9.1.62

Pitilakis, K., Gazepis, C., Anastasiadis, A., 2004. Design Response Spectra and Soil Classification for Seismic Code Provisions. Presented at the 13th World Conference on Earthquake Engineering, Vancouver, B.C., Canada.

Polese, M., Gaetani d'Aragona, M., Prota, A., 2019. Simplified approach for building inventory and seismic damage assessment at the territorial scale: An application for a town in southern Italy. Soil Dynamics and Earthquake Engineering 121, 405–420. https://doi.org/10.1016/j.soildyn.2019.03.028

Poulton, M.M., 2001. Computational neural networks for geophysical data processing. Elsevier.

Ravari, Z.A., Ghazi, I., Kahani, M., 2016. Study the vulnerability and blocking of streets after earthquake (case

study: Kerman Shariati and Shahid Beheshti Streets and Jomhuri Boulevard). Int J Health Syst Disaster Manage 4, 25–30. https://doi.org/10.4103/2347-9019.175673

Regnier, J., Cadet, H., Bonilla, L.F., Bertrand, É., Semblat, J.F., 2013. Assessing Nonlinear Behavior of Soils in Seismic Site Response: Statistical Analysis on KiK-net Strong-Motion Data. Bulletin of the Seismological Society of America 103, 1750–1770.

Riedel, I., Guéguen, P., 2018. Modeling of damage-related earthquake losses in a moderate seismic-prone country and cost–benefit evaluation of retrofit investments: application to France. Nat Hazards 90, 639–662. https://doi.org/10.1007/s11069-017-3061-6

Salameh, C., 2016. Ambient vibrations, spectral content and seismic damages : new approach adapted to the urban scale. Application on Beirut (Theses). Université Grenoble Alpes.

Salameh, C., Bard, P.-Y., Guillier, B., Harb, J., Cornou, C., Gérard, J., Almakari, M., 2017. Using ambient vibration measurements for risk assessment at an urban scale: from numerical proof of concept to Beirut case study (Lebanon). Earth, Planets and Space 69, 1–17. https://doi.org/10.1186/s40623-017-0641-3

Salameh, C., Guillier, B., Harb, J., Cornou, C., Bard, P.-Y., Voisin, C., Mariscal, A., 2016. Seismic response of Beirut (Lebanon) buildings: instrumental results from ambient vibrations. Bull Earthquake Eng 14, 2705–2730. https://doi.org/10.1007/s10518-016-9920-9

Salloum, N., Jongmans, D., Cornou, C., Youssef Abdel Massih, D., Hage Chehade, F., Voisin, C., Mariscal, A., 2014. The shear wave velocity structure of the heterogeneous alluvial plain of Beirut (Lebanon): combined analysis of geophysical and geotechnical data. Geophysical Journal International 199, 894–913. https://doi.org/10.1093/gji/ggu294

Santarelli, S., Bernardini, G., Quagliarini, E., 2018. Earthquake building debris estimation in historic city centres_ From real world data to experimental-based criteria. International Journal of Disaster Risk Reduction 31, 281–291.

Sarris, A., Loupasakis, C., Soupios, P., Trigkas, V., Vallianatos, F., 2010. Earthquake vulnerability and seismic risk assessment of urban areas in high seismic regions: application to Chania City, Crete Island, Greece. Natural Hazards 54, 395–412. https://doi.org/10.1007/s11069-009-9475-z

Schnabel, P.B., Lysmer, J., Seed, B., 1972. A computer program for earthquake analysis of horizontally layered sites (No. EERC 72-12). Earthquake Engineering Research Center, University of California, Berkely.

Silva, V., Brzev, S., Scawthorn, C., Yepes, C., Dabbeek, J., Crowley, H., 2022. A Building Classification System for Multi-hazard Risk Assessment. Int J Disaster Risk Sci 13, 161–177. https://doi.org/10.1007/s13753-022-00400-x

Silva, V., Crowley, H., Varum, H., Pinho, R., 2015. Seismic risk assessment for mainland Portugal. Bull Earthquake Eng 13, 429–457. https://doi.org/10.1007/s10518-014-9630-0

Sousa, L., Silva, V., Bazzurro, P., 2017. Using Open-Access data in the development of Exposure datasets of Industrial buildings for Earthquake Risk modelling. Earthq. Spectra 33, 63–84.

Takewaki, I., 1998. Remarkable response amplification of building frames due to resonance with the surface ground. Soil Dynamics and Earthquake Engineering 17, 211–218. https://doi.org/10.1016/S0267-

7261(98)00006-2

Tumurbaatar, Z., Miura, H., Tsamba, T., 2021. Development of Building Inventory Data in Ulaanbaatar, Mongolia for Seismic Loss Estimation. IJGI 11, 26. https://doi.org/10.3390/ijgi11010026

Wald, D.J., Quitoriano, V., Heaton, T.H., Kanamori, H., 1999. Relationships between peak ground acceleration, peak ground velocity, and modified Mercalli intensity in California. Earthquake spectra 15, 557–564.

Wald, D.J., Worden, C.B., Thompson, E.M., Hearne, M., 2022. ShakeMap operations, policies, and procedures. Earthquake Spectra 38, 756–777. https://doi.org/10.1177/87552930211030298

Walley, C.D., 1988. A braided strike-slip model for the northern continuation of the Dead Sea Fault and its implications for Levantine tectonics. Tectonophysics 145, 63–72. https://doi.org/10.1016/0040-1951(88)90316-2

Whitman, R.V., 1973. Damage probability matrices for prototype buildings (Department of Civil Engineering Research Report No. R73-57). Massachusetts Institute of Technology, Cambridge, Massachusetts.

Wieland, M., Pittore, M., Parolai, S., Zschau, J., Moldobekov, B., Begaliev, U., 2012. Estimating building inventory for rapid seismic vulnerability assessment: Towards an integrated approach based on multi-source imaging. Soil Dynamics and Earthquake Engineering 36, 70–83. https://doi.org/10.1016/j.soildyn.2012.01.003

Yassin, N., 2012. Beirut. Cities 29, 64–73. https://doi.org/10.1016/j.cities.2011.02.001

Statements & Declarations

Funding

This work was supported by the National Research Agency under the Future Investments program bearing the reference ANR-15-IDEX-02, the grant N°ANR-17-CE03-0007-03, the Agence Universitaire de la Francophonie through the PCSI program and the International Research Network O-Life between Lebanon and France (SA16/22).

Competing Interests

The authors have no relevant financial or non-financial interests to disclose.

Author Contributions

All authors contributed to the study conception and design.

Detailed contributions of each author are listed in the table below:

Contributions	**Author (s)**
Damage estimation	Rouba Iskandar, Bilal Al-Tfaily, Pierre-Yves Bard, Bertrand Guillier, Cécile Cornou, Jacques Harb and Christelle Salameh

Debris estimation	Jacques Harb, Pierre-Yves Bard, Bertrand Guillier, Cécile Cornou, Julie Dugdale and Rouba Iskandar
Acquisition of data	Pascal Lacroix, Jocelyne Adjizian-Gérard, Nada Saliba and Rita Zaarour
Analysis and interpretation of satellite images data	Pascal Lacroix and Rouba Iskandar
Supervision	Elise Beck, Cécile Cornou and Julie Dugdale

The first draft of the manuscript was written by Rouba Iskandar and all authors commented on previous versions of the manuscript. All authors read and approved the final manuscript.

Appendix

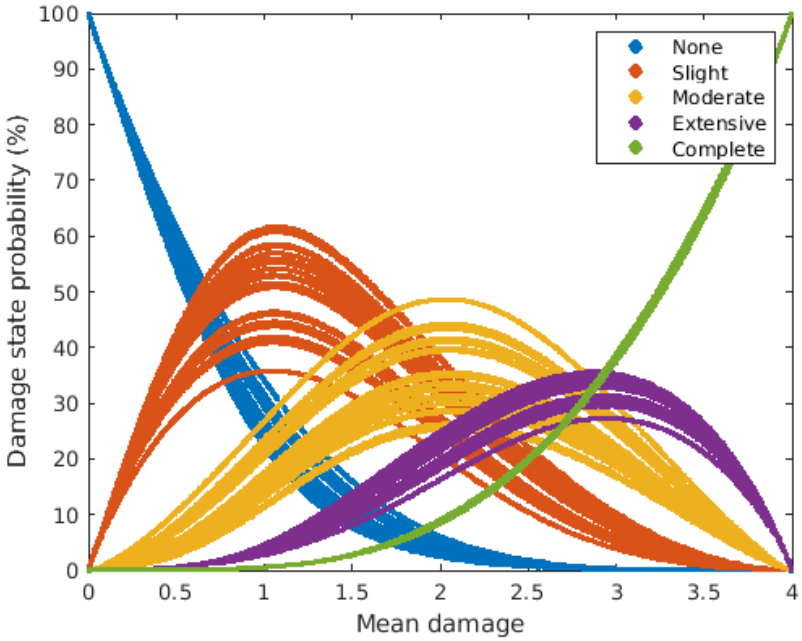

Fig. 21 Damage state probabilities depending on the mean damage value for buildings class 1

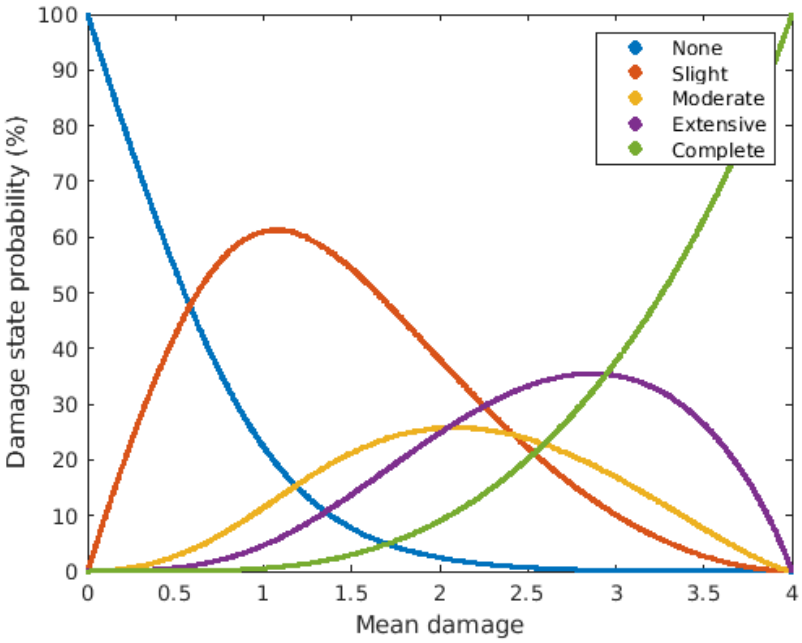

Fig. 22 Damage state probabilities depending on the mean damage value for buildings class 2

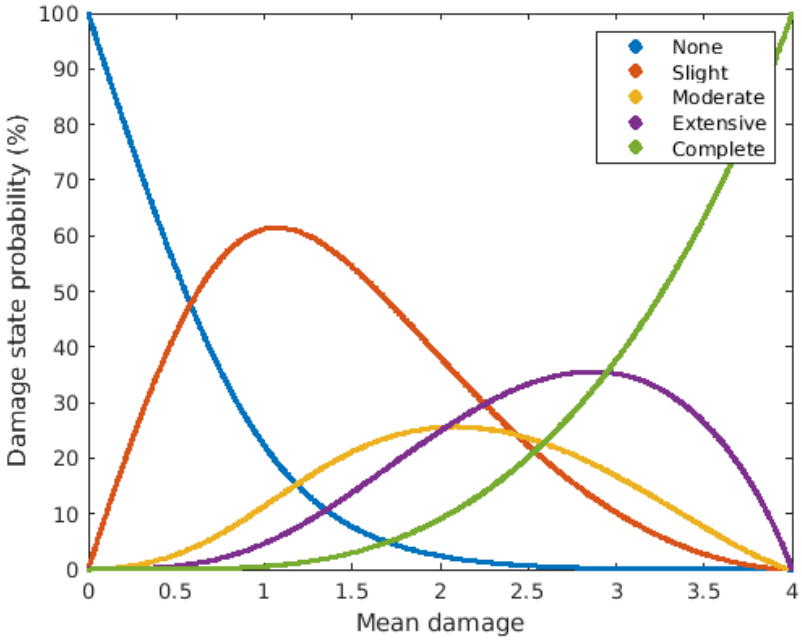

Fig. 23 Damage state probabilities depending on the mean damage value for buildings class 3

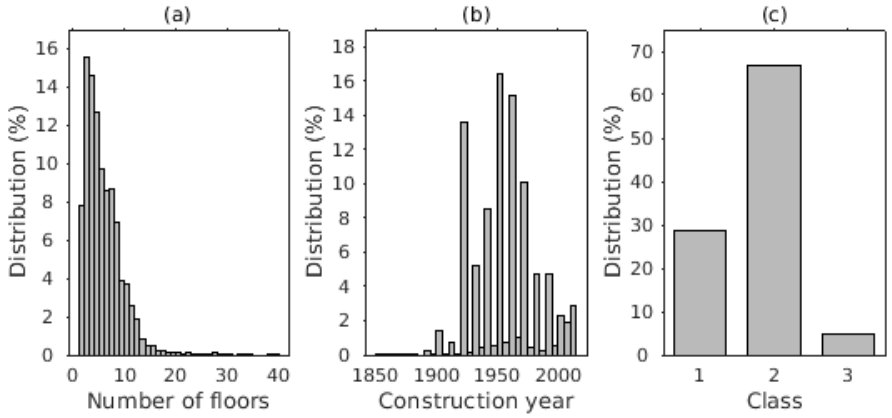

Fig. 24 Distribution of the characteristics of the buildings in Beirut surveyed in the framework of the LIBRIS project. (a) Number of floors, (b) construction year and (c) typology.

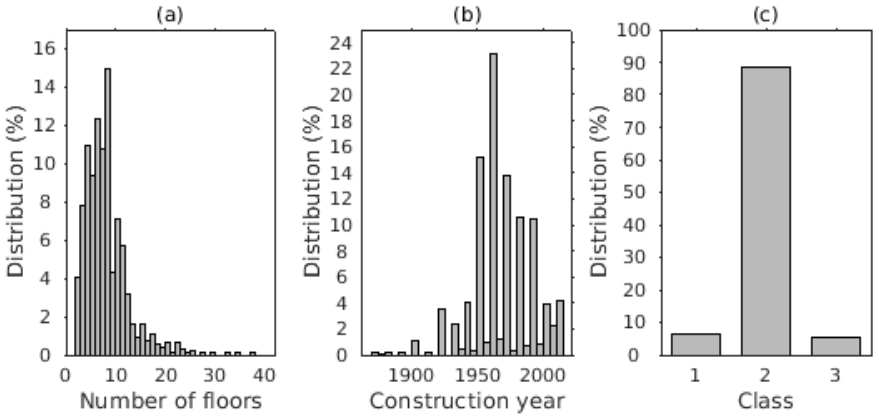

Fig. 25 Distribution of the characteristics of the subset of buildings in Beirut retained for the statistical analysis (LIB-STAT). (a) Number of floors, (b) construction year and (c) typology

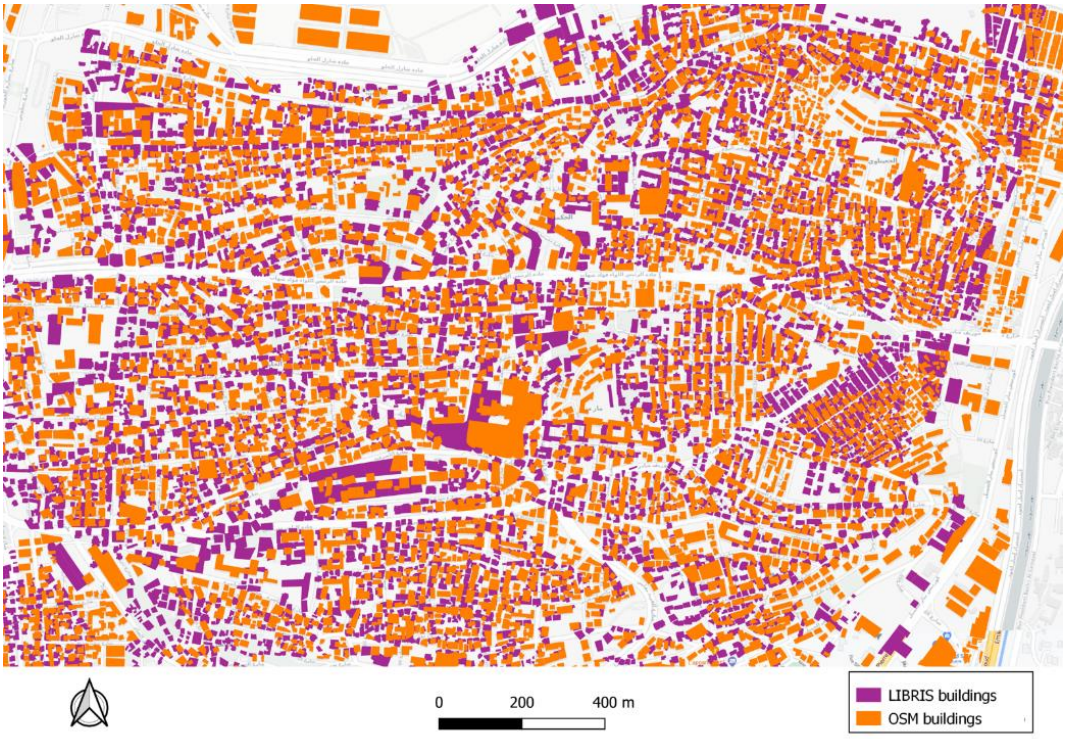

Fig. 26 Geolocalisation incompatibilities between the LIBRIS buildings (purple) and the OSM buildings (orange)

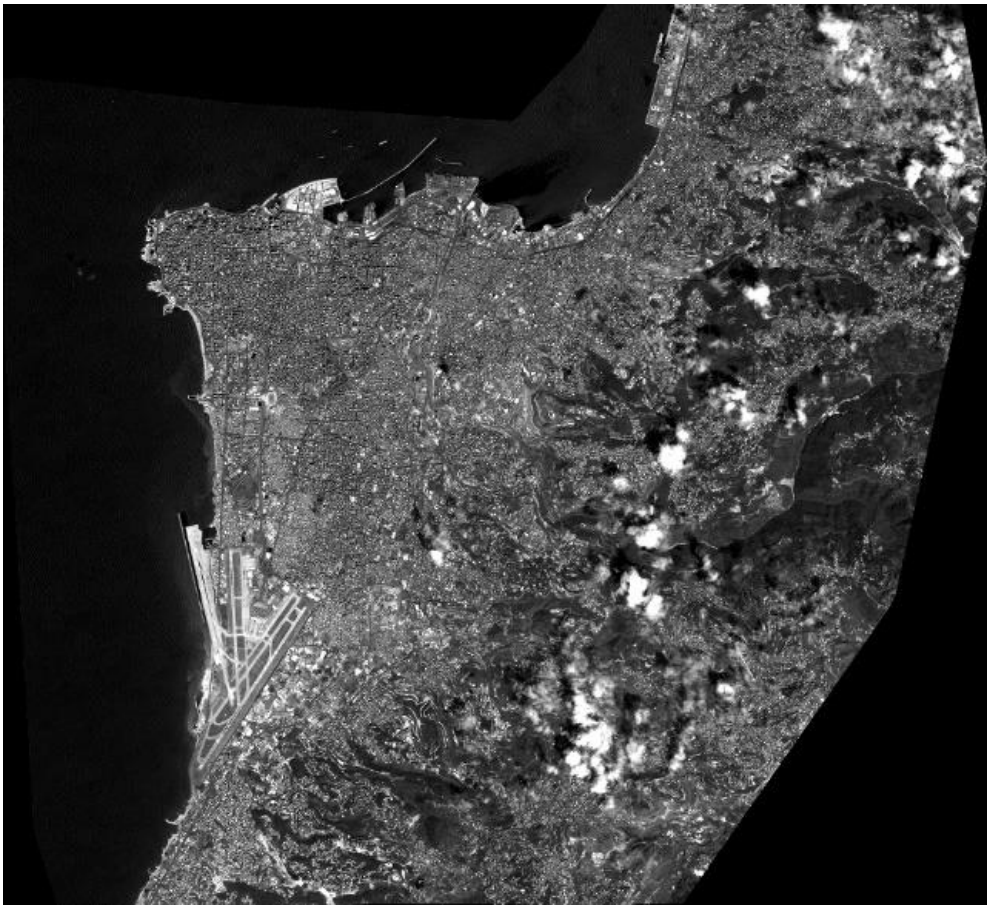

Fig. 27 Preview of one of the Pleiades 1-B panchromatic satellite images taken over Beirut

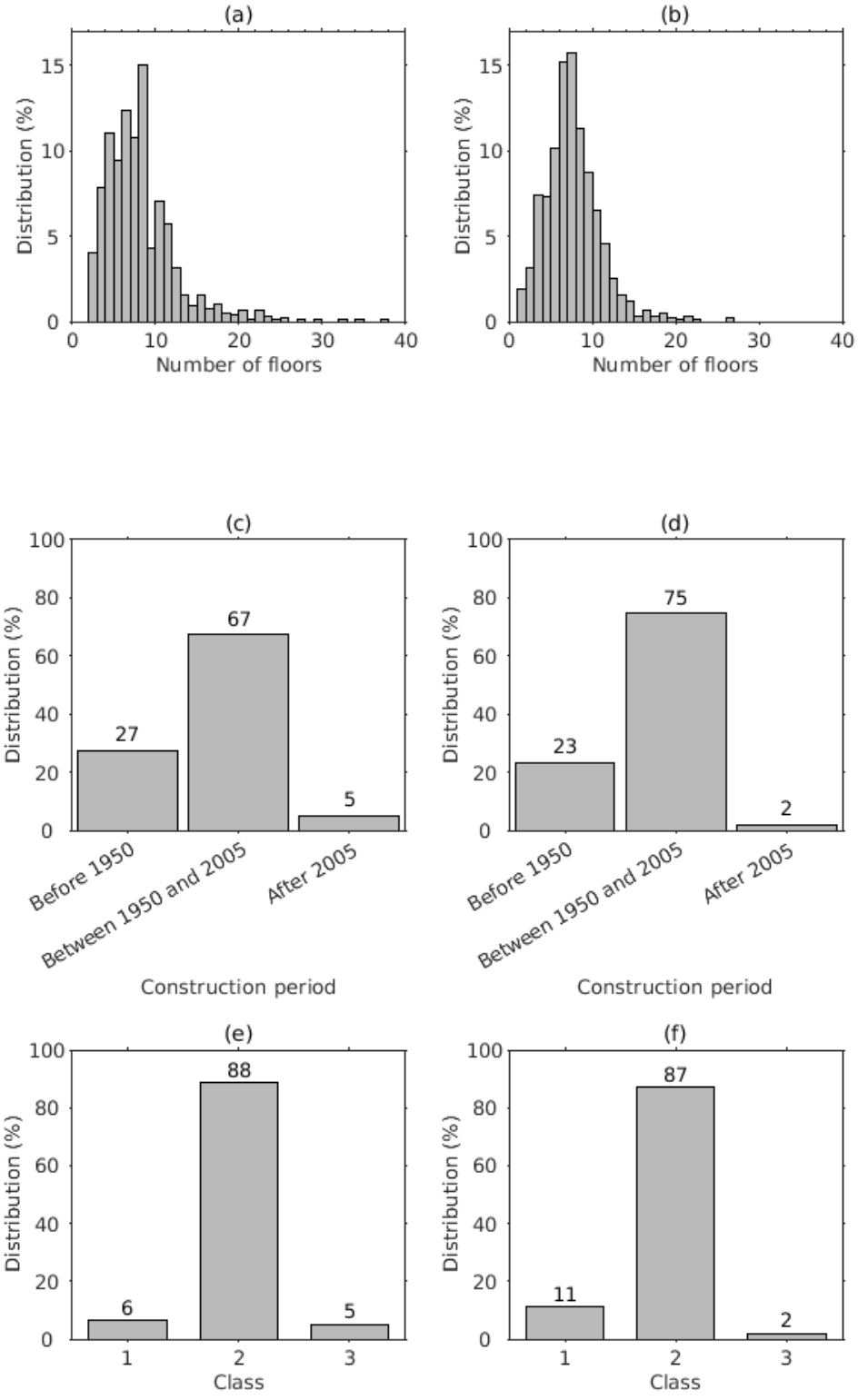

Fig. 28 Detailed comparison of the distribution of the characteristics of the original and predicted characteristics of the LIB-STAT dataset. (a) Original number of floors distribution, (b) Predicted number of floors distribution, (c) Original construction

period distribution, (d) Predicted number of floors distribution, (e) Original typology distribution, (f) Predicted typology distribution